Voltage-Assisted Differentially Grown Zinc Oxide Nanowires based Two Terminal Device for Sensing Applications

Thesis submitted towards partial fulfilment of the requirements for the award of the Degree of:

Master of Technology in Nano Science and Technology

Submitted By:

GOURAB PAYRA

Registration number: 163806 of 2022-2023

Class Roll No.: 002230701001

Examination Roll No.: M4NST24001

Under the guidance of

Dr. Chandan Kumar Ghosh

School of Materials Science and Nanotechnology
Jadavpur University
Kolkata-700032
INDIA

Course affiliated to:
Faculty of Interdisciplinary Studies, Law and Management
Jadavpur University
Kolkata-700032
INDIA

August 2024

M.Tech. (Nanoscience and Technology)
Course affiliated to:
Faculty of Interdisciplinary Studies, Law and Management
Jadavpur University Kolkata, India

CERTIFICATE OF RECOMMENDATION

We hereby recommend that the thesis entitled as "Voltage-Assisted Differentially Grown Zinc Oxide Nanowire based Two Terminal Device for Sensing Applications", prepared by Mr. Gourab Payra (Class Roll No: 002230701001, Registration No: 163806 of 2022-2023, Examination Roll No: M4NST24001) under our guidance, be accepted in partial fulfilment of the requirement for the award of the Degree of Master of Technology in Nano Science and Technology from the School of Materials Science and Nano Technology of Jadavpur University.

HOD/Director

Dr. Mahua Ghosh Chaudhuri
Director,
School of Materials Science & Nanotechnology,
Jadavpur University

Thesis Advisor

Dr. Chandan Kumar Ghosh
Professor,
School of Materials Science & Nanotechnology,
Jadavpur University

Dean-FISLM,
Jadavpur University,
Kolkata-700032

M.Tech. (Nanoscience and Technology)
Course affiliated to:
Faculty of Interdisciplinary Studies, Law and Management
Jadavpur University Kolkata, India

CERTIFICATE OF APPROVAL

I hereby endorse the foregoing as an engineering study, conducted and presented in a manner satisfactory enough to justify its acceptance as an engineering study, in order to obtain the degree for which it has been submitted. This approval does not endorse or approve any statements made, opinion expressed or conclusion drawn therein but merely approve the thesis for the purpose for which it has been submitted.

Committee of the final examination for evaluation of the Thesis

ACKNOWLEDGEMENT

I would like to express my deepest gratitude to my supervisor, Dr. Chandan Kumar Ghosh, Assistant Professor, School of Materials Science and Nanotechnology, Jadavpur University, for his guidance, invaluable expertise and constant support throughout this research endeavour. His guidance has been invaluable in developing this thesis and my progress as a student.

I am immensely grateful to Dr. Sayan Dey, Assistant Professor, School of Electrical Sciences, IIT Bhubaneswar, for his continuous support and motivation throughout this journey. His insightful inputs and assistance have been invaluable in overcoming challenges and pushing the boundaries of this research.

I gratefully thank Prof. Kalyan Kumar Chattopadhyay, Dr. Sourav Sarkar and Dr. Mahua Ghosh Chaudhuri, for their assistance, support, recommendations and guidance. They offered a helpful and constructive learning environment, and their excitement inspired me to pursue the research topic with zeal.

I would like to acknowledge and thank all the members of the Nano Lab, including Sourav Kumar Nandi, Panchanan Sahoo, Sudip Kundu, Riddhiman Sahoo, Mandira Das, Shriya Purokait, Raushan Kabir Khan, Roshni Begum, Kazi Wakar Hasan, Srijita Chakraborty, Debadrita Bhaduri, and others, for their collaborative spirit, technical assistance, and stimulating discussions that have enriched my research experience.

I would also like to thank Amrita Roychowdhury and Manash Thakur for their technical support on my study.

I am grateful to the members of the VLSI Lab, Department of Electronics and Communication Engineering, School of Electrical Sciences, IIT Bhubaneswar, including Shreyansh Mishra, Sukanya Mahalik, Mrinmay Patra, Anuvindh R., Arijit Patra and Piyush Chankapure, for their support and guidance in various aspects of my work.

Lastly, I would like to express my deepest appreciation to my parents for their unwavering faith, unconditional love, support and encouragement throughout my academic journey. Their belief in me has been a constant source of strength and inspiration. I am grateful to everyone mentioned above, as well as any individuals who have contributed to this research in any way, for their invaluable support, which has been instrumental in the successful completion of this thesis.

-Gourab Payra

Dedicated to my Parents

ABSTRACT

Zinc oxide is considered an intriguing semiconductor alternative to the typically employed semiconductors. As it provides high thermal and chemical stability, a wide energy bandgap, a high electrochemical coupling coefficient, and biocompatibility, it also has a wide range of morphologies that can be used various applications. Among them, the ZnO nanowire is one of the most researched morphologies.

There are different synthesis methods available for ZnO nanowire growth. In this work, a modified Chemical Bath Deposition method was implemented for ZnO nanowire formation. As the Chemical Bath Deposition is a bottom– up solution based synthesis method, it has different ions in the solution. By applying external voltage, the ion distribution can be manipulated. So a voltage-Assisted Chemical Bath Deposition method was implemented to form ZnO nanowire on a Silicon substrate. As different growth condition may effect the growth of nanowires, without changing other parameters only changing the applied voltage four devices were fabricated. Different characterisation methods such as X-Ray Diffraction (XRD) and FESEM imaging for its morphological study , Diffuse Reflectance Spectroscopy(DRS) for its optical properties, and Voltage current characteristics for electrical properties, were performed to analyse the ZnO nanowire grown on the silicon substrate and the effect of the different applied voltages. This study demonstrated the effect of voltage assisted chemical bath deposition methods on nanowire growth.

To study the Chemiresistive application of the fabricated device, the device was tested against Cu (II), Cr(III),Fe(II) and Ni(II) heavy metal ions. The comparative data for four devices were analyse using current response of the devices in presence of each heavy metal ions. It was established that this device can be used as a chemiresistive sensor for Cu (II) ions.

Keywords: ZnO Nanowires, Chemical Bath Deposition(CBD), Voltage –assisted Chemical Bath Deposition, Chemiresistive sensor, Heavy metal Sensor

.

TABLE OF CONTENT

ACKNOWLEDGEMENT IV

ABSTRACT VI

LIST OF FIGURES IX

LIST OF TABLES XI

ABBREVIATIONS XII

SYMBOLS

Chapter - 1 XIII

1. INTRODUCTION 2
   1.1. Background 2
   1.2. Objective 3
   1.3. Outline 3

Chapter - 2

2. LITERATURE REVIEW 5
   2.1. Zinc Oxide(ZnO) 5
      2.1.1. Physical Properties 7
      2.1.2. Defects and Emission Properties 8
      2.1.3. Electrical properties 10
      2.1.4. ZnO Growth Methods 11
         2.1.4.1. Gas Phase ZnO Growth Methods 11
         2.1.4.2. Liquid Phase ZnO Growth Methods 16
            2.1.4.2.1. Chemical Bath Deposition(CBD) 18
      2.1.5. Applications 23
         2.1.5.1. Solar Cell 24
         2.1.5.2. Light Emitting Diodes(LEDs) 24
         2.1.5.3. Ultraviolet Detector 24
         2.1.5.4. Nanogenerators 25
         2.1.5.5. Field Emission Devices 25
         2.1.5.6. Photocatalysis 26
         2.1.5.7. Sensors 26
   2.2. Sensors 27
      2.2.1. Chemical Sensors 27
         2.2.1.1. Sensor Parameters 27
      2.2.2. Heavy Metal Ion Sensors 28
   2.3. Heavy Metals 29

2.3.1. Copper(Cu) 28
2.3.2. Chromium(Cr) 28
2.3.3. Iron(Fe) 28
2.3.4. Nickel(Ni) 29

Chapter - 3

3. METHODOLOGY 33
3.1. FABRICATION 33
3.1.1. Materials and Instruments 33
3.1.2. ZnO Growth Process 33
3.1.2.1. Substrate Preparation 34
3.1.2.2. Double Step Chemical Bath Deposition (CBD) Method for Synthesis of ZnO Nanowire 34
3.1.2.3. Variation of Growth Parameters 39
3.2. CHARACTERISATION 39
3.2.1. X-Ray Diffraction (XRD) 39
3.2.2. Diffuse Reflectance Spectroscopy(DRS) 40
3.2.3. Field Emission Scanning Electron Microscope (FESEM) 42
3.2.4. Current – Voltage Characteristics 42
3.3. HEAVY METAL DETECTION 42

Chapter - 4

4. RESULTS AND DISCUSSIONS 44
4.1. Structural and Morphological Properties 45
4.1.1. X-Ray Diffraction analysis 45
4.1.2. Field Emission Scanning Electron Microscopy(FESEM) 51
4.2. Optical Properties 52
4.2.1. Diffuse Reflectance Spectroscopy(DRS) Analysis 52
4.3. Electrical Properties 56
4.4. Heavy Metal Ions Detection 61

Chapter - 5

5. CONCLUSION AND FUTURE WORK 66
5.1. CONCLUSION 66
5.2. FUTURE WORK 67

Chapter - 6

6. REFERENCES 67

LIST OF FIGURES

Fig2.1 The hexagonal wurtzite structure of ZnO. The red circle represents the zinc ions and white circle represents the oxygen ions coordinated tetrahedral.

Fig 2.2 a simple schematic diagram explaining the Pulse Laser Deposition process

Fig 2.3 Schematic diagram describing Sputtering deposition process

Fig 2.4 Schematic diagram illustrating a Molecular beam epitaxy system.

Fig 2.5 a simple diagram representing the Chemical Vapour deposition (CBD) process

Fig 2.5 Schematic diagram to present the steps required for Solvothermal synthesis process.

Fig 2.6 A simple schematic diagram representing a setup for Chemical Bath deposition process.

Fig 2.7 Various Applications of Zinc Oxide Nanowires

Fig 3.1: A Silver Paste deposited p-Si (100) substrate

Fig3.2 (A) Simple schematic diagram of the Voltage-Assisted Chemical Bath Deposition (CBD) method

(B) Experimental Setup for the Voltage-Assisted Chemical Bath Deposition (CBD) method

Fig 3.3 Flow Diagram of The ZnO seed layer growth procedure

Fig 3.4 Flow diagram of the Step 2: ZnO nanowire development

Fig 4.1 The Devices fabricated using Voltage-assisted double chemical Bath Deposition.

(A) SET 1(V2.5); (B) SET 2(V5.0); (C) SET 3(V7.5); (D) SET 4(V10.0)

Fig 4.2 XRD pattern of the ZnO Nanowire grown on Silicon Substrate using Voltage-Assisted Chemical Bath Deposition (CBD). SET 1(V2.5), SET 2(V5.0), SET 3(V7.5), and SET 4(V10.0) are the 4 fabricated devices

Fig 4.3 the FESEM image of the device SET 2 (V5.0). (A) image of the section SET 2 (pV5.0) (B) image of the section SET 2 (nV5.0)

Fig 4.4 Reflectance spectra of the devices

(A) SET 1(V2.5); (B) SET 2(V5.0); (C) SET 3(V7.5); (D) SET 4(V10.0)

Fig 4.5 Bandgap energy (Eg) calculation from Tauc plot for determining the bandgap energy of both ends of the devices

Fig 4.6 Voltage-current (I-V) characteristics of four devices SET 1(V2.5); (B) SET 2(V5.0); (C) SET 3(V7.5); (D) SET 4(V10.0)

Fig 4.7 The drawing of the equivalent circuit of the device designed in Pspice software

Fig 4.8 circuit design for I-V characteristics of a diode

From the Fig 4.9, it can be deducted that both end of the device may act like Zener diode.

Fig 4.10 Cu(II), Cr(III), Fe(III) and Ni(II) sensing using SET 1(V2.5)

(a) Response, (b) Selectively

Fig 4.11 Cu(II), Cr(III), Fe(III) and Ni(II) sensing using SET 2(V5.0)

(a) Response, (b) Selectively

Fig 4.12 Cu(II), Cr(III), Fe(III) and Ni(II) sensing using SET 3(V7.5)

(a) Response, (b) Selectively

Fig 4.13 Cu(II), Cr(III), Fe(III) and Ni(II) sensing using SET 4(V10.0)

(b) (a) Response, (b) Selectively

LIST OF TABLES

Table 2.1 Basic physical properties for ZnO at ambient temperature

Table 3.1 Variation in growth parameters during fabrication process

Table 4.1 List of peaks found in XRD pattern and the materials and planes associated with them

Table 4.2 Comparison of Crystalline size using Scherrer's Equation and Williamson-Hall Plot

Table 4.3 Bandgap energy (Eg) calculation from Tauc plot for determining the bandgap energy of both ends of the devices SET 1(V2.5), SET 2(V5.0) , SET 3(V7.5), SET 4(V10.0).

Table 4.4 comparison between IV characteristics of the devices and their equivalent circuit

Table 4.5 List of standard reduction potential of Cu(II), Cr(III), Fe(III) and Ni(II)

ABBREVIATIONS

LED – light emitting diode

CBD- chemical bath deposition

CB- conduction band

VB- valance band

FWHM – Full width at Half maxima

UV- ultraviolet

PLD pulsed laser deposition

MBE- Molecular beam epitaxy

CVD- chemical vapour deposition

NW- Nanowire

XRD – X-Ray Diffraction

I-V- Current-voltage

JCPDS - Joint Committee on Powder Diffraction Standards

SYMBOLS

Si – silicon

ZnO- Zinc oxide

Θ – Bragg's angle

N – frequency

γ Factor(Tauc method)

β- full width at half-maximum (FWHM)

λ- wavelength

σ- strain

α- absorption coefficient

Å-angstrom

nm - nanometre

μm-micrometr

Chapter-1:

INTRODUCTION

1. INTRODUCTION

1.1 Background

Nowadays, semiconductor devices have become a crucial and essential component of our everyday lives, and we can't imagine living without them. The present scientific achievement in semiconductor devices based on various semiconducting materials is the foundation of the modern electronics industry, which includes high-tech computers, televisions, mobile phones, and a variety of other products. Furthermore, the modern industrial trend is to miniaturise electronic devices and increase their efficiency. The semiconductor silicon (Si) maintains its dominant position in the modern electronic industry, as it is used to fabricate discrete and very large scale integrated circuits (VLSI) for various applications. Furthermore, Si is not an optimal material for optoelectronic devices due to its indirect band gap, such as white light emitting diodes (LEDs). To overcome this problem GaAs with direct band gap was chosen. The fast growth of information technology has led to a significant increase in the demand for ultraviolet (UV) and blue light emitters, which exceeds the capabilities of GaAs. Scientists are increasingly interested in so called third-generation semiconductors like SiC, GaN, and ZnO due to their unique properties in the semiconductor industry.

Researchers have developed a variety of nanostructured metal oxide (e.g., nanowires, nanorods, and nanoflowers) that improve the sensitivity and selectivity of gas sensors while lowering recovery/response times and operating temperatures (1). ZnO nanostructures' exceptional characteristics (electro-optical, piezoelectric, luminescence, biocompatibility, and long-term stability) have led to its application in energy conversion, environmental monitoring, and chemical/biological sensing (2)(3)(4).

In light of the fast rise of industry and transportation, concerns of environmental contamination by heavy metals, notably lead, mercury, cadmium, and cobalt, are becoming increasingly relevant. Many metals create stable organic compounds that dissolve well in water and cause heavy metal ions to migrate in aquatic and terrestrial systems, resulting in high levels of pollution (5)(6). ZnO nanostructures are interesting opportunities for use in these sensors. They are sensitive to a wide range of contaminants, including practically all heavy metal ions and organic pollutants, and exhibit excellent adsorption results for the most dangerous ions (Pb, Cd, Hg). In general, ZnO is chemically inactive; therefore it will not

constitute a secondary source of contamination. Furthermore, ZnO nanostructures can have a variety of morphologies, allowing you to tailor the electrical and optical characteristics of the nanostructured layer to a specific application without changing the real material. In contrast to needle-shaped nanostructures, other varieties of ZnO nanostructures have received less attention, and study into such structures might lead to new uses(7).

1.2 OBJECTIVE

The aim of this thesis is to develop a two terminal device using Zinc Oxide (ZnO) nanowire as a sensing material. There are many top-down and bottom-up approaches available for synthesising ZnO Nanowires. In this thesis, a bottom-up approach was implemented to grow Nanowire on Silicon (Si) substrate using the voltage-assisted chemical bath deposition (CBD) method. Here, a double chemical bath deposition method was used to get certain morphologies. The first CBD is used to form a seed layer on the Silicon(Si) substrate and the second CBD is used to control the further growth of the ZnO nanowire on the seed layered substrate. Also, different voltage levels were used to fabricate those devices. The aim of this process was to change the synthesis conditions so that devices with different characteristics could be fabricated. The primary goal was to fabricate a heterojunction two-terminal device that can be used as Chemiresistive sensor and use it to sense different heavy metals and volatile organic compounds (VOCs).

1.3 OUTLINE

In ‘Literature review’ a brief review work was done on the Zinc oxide(ZnO) as sensing material and its different synthesis methods and application, also its detailed Chemiresistive application included, a detailed explanation on the target materials(i.e. few heavy metals) also was covered. In device fabrication, a voltage-assisted chemical bath deposition method was implemented, where a few devices were fabricated by changing the growth condition, mainly the applied voltage. The goal was to observe the effect of the applied voltage in the fabrication method and characterise those changes due to those different applied voltage. Next, those fabricated devices were used to detect heavy metals in water, where the selectivity and sensitivity of those devices were characterised.

Chapter-2:

LITERATURE REVIEW

2. LITERATURE REVIEW

In this section, a brief explanation of zinc oxide, its properties, and its application, along with sensors and heavy metals, is provided.

2.1. Zinc Oxide(ZnO)

ZnO has a hexagonal (wurtzite) crystal structure with lattice parameters a = 3.25 Å and c = 5.12 Å. The significant difference in electronegativity (Oxygen = 3.44 and Zinc = 1.65) is responsible for the strong ionic interaction between them. In wurtzite formations, zinc (Zn) atoms are tetrahedral in coordination with four oxygen (O) atoms stacked alternatively along the c-axis. In general, the ZnO unit cell is neutral, with one oxygen anion surrounded by four zinc cations at each corner of a tetrahedron, and vice versa. The distribution of cations and anions can assume particular arrangements as established by crystallographic techniques, resulting in positively or negatively charged surfaces known as polar surfaces. These polar ZnO surfaces consist of nontransferable and unchanging ionic charges, and their surface interaction is determined by their distribution. As a result, the structures have been formed with little electrostatic energy, allowing for the creation of polar surface-dominated nanostructures. This amazing phenomenon leads to the construction of various ZnO one-dimensional (1D) nanostructures such as nanowires, nanorods, nanotubes, nanospring, nanocages, nanobelts, and so on (8).

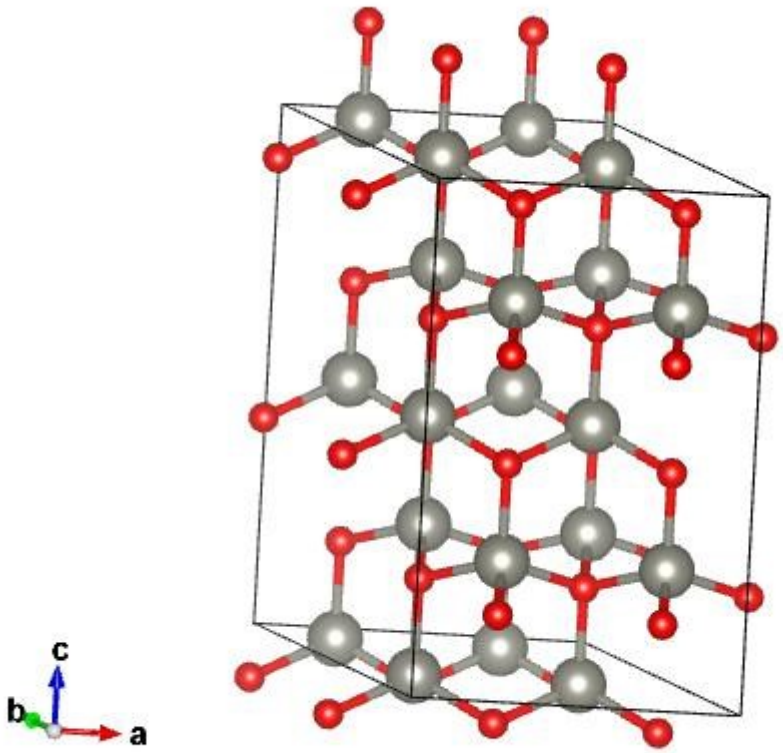


Fig2.1 The hexagonal wurtzite structure of ZnO. The red circle represents the zinc ions and white circle represents the oxygen ions coordinated tetrahedral.

The wurtzite structure of ZnO has four common surfaces: two polar (Zn (0001) and O (000$\bar{1}$) with terminated faces along the c axis, and two non-polar (11 20) and (10$\bar{1}$0) faces with an equal number of zinc (Zn) and oxygen (O) atoms. ZnO has distinct chemical and physical characteristics because to its polar surfaces. The most frequent polar surface is the basal plane. In the presence of polarised charged ions, distinct surfaces, such as positively charged Zn-(0001) and negatively charged O-(000 1) polar surfaces, are formed, resulting in a normal dipole moment, spontaneous polarisation along the c-axis, and a divergence in surface energy. Polar surfaces often contain facets or extensive surface reconstructions to ensure stability. However, ZnO (0001) and (000$\bar{1}$) are exceptions since it is atomically flat, stable, and does not require reconstruction (9). At comparatively low external hydrostatic pressures, ZnO can be converted into rocksalt (NaCl) structures in addition to wurtzite. At around 10

GPa, ZnO undergoes a pressure-induced phase shift from wurtzite (B4) to rock salt (B1) (10). ZnO has various benefits over existing devices constructed of other wideband semiconductors, the most prominent of which is its high exciton binding energy of 60 meV at ambient temperature, as opposed to its equivalent GaN (25 meV). This increased exciton binding energy is responsible for increasing the efficiency of light emission (11).

2.1.1. Physical Properties

Table 2.1 shows a few basic physical properties for ZnO at ambient temperature (11-15).

NO	**Parameters**	**Values**
1	Lattice constants at 300 K	a = 0.32495 nm, c = 0.52069 nm
2	Molecular mass	81.389 g/mol
3	Density	5.67526 g/cm^3
4	Melting point	2250 K
5	Hole effective mass	0.59 m_0
6	Electron effective mass	0.28 m_0
7	Static dielectric constant	8.656
8	Bandgap energy at 300 K	~3.37 eV
9	Refractive index	2.008, 2.029
10	Exciton binding energy	60 meV
11	Thermal conductivity	0.6 – 1.16 W/Km
12	Specific heat	0.125 cal/g°C
13	Electron mobility	~210 cm^2/Vs
14	Thermal constant	1200 mV/K

Table 2.1 Basic physical properties for ZnO at ambient temperature.

2.1.2. DEFECTS AND EMISSION PROPERTIES

The opto-electric characteristics of semiconductor materials are primarily determined by the intrinsic and extrinsic defects present in their crystal structures. Researchers have recently focused on the optical properties of ZnO, particularly ZnO nanostructures, due to its wide band-gap (~3.37 eV at room temperature), making it a promising material for photonic applications in the UV or blue spectral range. Additionally, the high exciton-binding energy (60 meV), which is much larger than that of GaN (25 meV), allows for efficient excitonic emission even at room temperature. ZnO's efficient radiative recombinations have made it a

desirable material for optoelectronics applications. The PL spectra indicated an ultraviolet (UV) emission band as well as a large visible emission band. The UV peak is often noticed as a result of transition recombination of free excitons (F.E) at the band edge of ZnO. Excitons may have behaviours, such as being free and able to flow through the crystal or being bound to donors and accepters with neutral or charged states (16). Changes in the optical and electrical characteristics of ZnO can be caused by deep level defects in its crystal structure. These flaws can be created during the synthesis process or by other procedures like as post-annealing or ion implantation. The cause of intrinsic emission from ZnO is particularly debatable due to the existence of native point defects in the structure. The ZnO structure has donor and accepter energy levels, which are located below and above the conduction band (CB) and valence band (VB), respectively, and are responsible for near-band edge emissions. The emission of the whole visible area (400-750 nm) is caused by the presence of distinct deep energy levels contained within the bandgap (11, 16-26). There are three types of defects seen in the crystal structure: line defects, point defects, and complex defects. Line defects resulted from interruptions in atom rows, whereas point defects are caused by solitary atoms in localised regions, and complex defects are created when many point defects merge. Extrinsic point defects occur when impurities/foreign atoms are absorbed into the structure, whereas intrinsic defects only affect the host atoms. The intrinsic optical recombination happened between the electrons and holes present in the CB and VB respectively (17). Furthermore, the deep level emission (DLE) band or the whole visible range (400-750 nm) in ZnO has previously been linked to the existence of numerous inherent flaws in the structure, such as the oxygen vacancies (VO), oxygen interstitial (Oi), zinc vacancies (VZn) , zinc interstitial (Zni) and oxygen anti-site (OZn) and zinc anti-site (ZnO) (24-37). ZnO crystal structures have two distinct types of intrinsic vacancy defects: oxygen vacancy (Vo) and zinc vacancy (Vzn). The green emission from ZnO is caused by the existence of single ionised oxygen vacancies. However, in the event of zinc-rich growth, the oxygen vacancy has lower formation energy than the zinc interstitial and dominates, whereas doubly ionised oxygen vacancies are responsible for the red emission from ZnO (38). The zinc vacancies are additionally believed to be the main source of blue emission in ZnO. The blue emission is caused by recombination between the zinc interstitial (Zni) and Vzn energy levels, which corresponds to about 2.84 eV (436 nm). The two most common defects found in ZnO structures are oxygen interstitial (Oi) and zinc interstitial (Zni). Zinc interstitial defects, located at ~ 0.22 eV below the CB, contribute significantly to visible emissions in ZnO

through recombination between Zni and other deep-level defects such as oxygen and zinc vacancies. Oxygen interstitials are the primary source of blue, red, and green emissions in ZnO (39). Oxygen interstitial defects are typically located at 2.28 eV below the CB and produce orange-red emissions in ZnO. Oxygen interstitial defects are also responsible for yellow emission (40-42). Anti-site defects are defects that occur in the ZnO structure as a result of occupying the incorrect lattice location, such as when zinc occupies the oxygen position or oxygen fills the zinc position in the lattice. A few more kinds of defects exist in ZnO, such as cluster defects, which result from the merger of several point defects. Such cluster defects may also be developed when the point and extrinsic defects such as VO Zni cluster, which is formed because of to the merger of oxygen vacancy and zinc interstitial, and it has been reported that it has a location at 2.16 eV below the CB (34).

Subsequently the extrinsic defects also can explain some other emission characteristics of ZnO. Ü. Özgür et al. explained in their work that Excitons bonded to extrinsic defects such as Li and Na accepters in ZnO structures cause UV emissions at 3.35 eV (17). The emission from copper impurities in ZnO is measured at 2.85 eV. Similarly, after doping Li in ZnO thin film, a yellow emission was seen at 2.2 eV below the CB with the Li-related defects (43-44). The emission spectra obtained from ZnO showed that it has a high potential to generate luminescence over the whole visible range and has an excellent prospects as a low-power white light generating source.

2.1.3. Electrical Properties Of ZnO

The electrical behaviour of ZnO nanostructures is crucial in determining their suitability for use in Nano-devices and Nanoelectronics. Ü. Özgür et al. explained in their work that Undoped ZnO nanostructures are typically n-type, as documented in the literature, due to the existence of native defects in their crystal structure, such as oxygen vacancies and zinc interstitials. The numerical values of the electron mobility in a ZnO nanostructures in an undoped condition are estimated 120 to 440 cm2 V/s at ambient temperature, which may also change as various synthesis methods produce variable morphology, which could impact the parameter (17). It has also been reported that following doping of ZnO, the maximum carrier concentration for holes and electrons, i.e., 10^19 cm-3 and 10^20 cm-3, were attained. The

carrier mobility has decreased when compared to the undoped ZnO caused by the carrier scattering mechanism, which comprises ionised impurity, non-ionized impurity, polar optical-phonon, and acoustic phonon scatterings (17). At room temperature, electron and hole mobility was predicted to be 200 cm2 V/s and 5–50 cm2 V/s, respectively. Similarly, the effective mass of electrons and holes were calculated to be 0.24 and 0.59 m0, respectively. As a result of the significant variations in their effective masses, holes have far lower mobility than electrons (45). ZnO is naturally an n-type semiconductor, owing to the following inherent and extrinsic defects: oxygen vacancies (v0), zinc interstitials (Zni), hydrogen interstitials (Hi), and substitutional hydrogen (H0). The substantial number of n-type defects makes it difficult to achieve consistent p-type conductivity in ZnO. Certain defects and dopants can enhance p-type behaviour, such as Zinc Vacancies (vzn), Oxygen Interstitials (oi), Group I (Li, Na, K) Dopants, and Group V (N, P, As) Dopants(17, 46-51).

2.1.4. ZnO Growth Methods

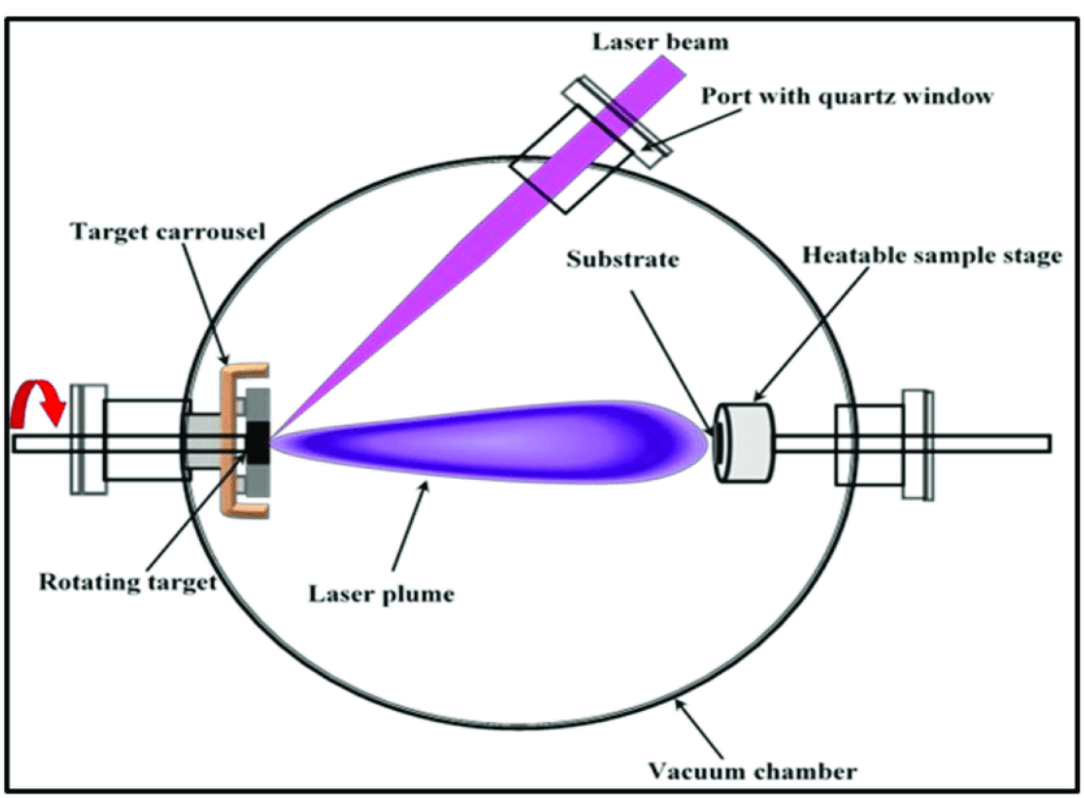
Zinc oxide can be synthesised in a vast array of morphologies by using a vast range of methods. Here, the use of these deposition techniques towards the growth of different ZnO morphologies is detailed. Depending on the desired application and morphology, different techniques have their uses. In this regard, the chemical bath deposition (CBD) of ZnO nanostructures is the most attractive due to its lower complexity, process flexibility, low cost, and adequate quality of the produced material. Considering this, ZnO nanowires (NWs) have become one of the most studied ZnO morphologies.

2.1.4.1. Gas phase ZnO growth methods

A simplistic categorisation of ZnO deposition methods may be established by considering their working phase, such as liquid or gas phase development. While liquid phase methods are generally utilised for the creation of any dimension (3D, 2D, or 1D) nanomaterials, gas phase techniques are mostly employed for two-dimensional (2D) materials

(thin films). Gas phase methods require that the zinc precursor be in the gas phase prior to deposition.

Pulsed Laser Deposition (PLD) - A gas phase method is pulsed laser deposition (PLD), a kind of physical vapour deposition. ZnO thin film deposition using PLD is based on the ablation of a ZnO target (52), also a precursor, such dimethylzinc, within a vacuum chamber that includes an inert gas (i.e. argon or nitrogen) and a reactive background gas (oxygen or a gas phase oxide) that works as an oxygen donor (53). To ablate the subject, a high intensity pulsed laser is employed. The as-deposited films' characteristics may be modified by tweaking the laser energy and wavelength, the pulse repetition rate, the number

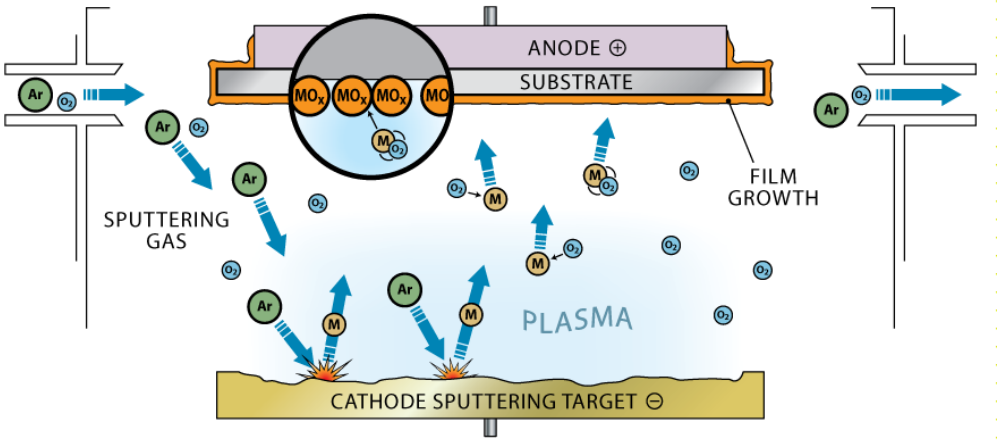


of pulses, and the substrate temperature.

Fig 2.2 a simple schematic diagram explaining the Pulse Laser Deposition process.

(Source-https://www.sputtertargets.net/blog/an-introduction-to-pulsed-laser-deposition-pld.html)

Sputtering - Sputtering is another method often used to produce ZnO thin films. In summary, inert gas plasma (typically argon) is created in a vacuum chamber containing a ZnO target. When this plasma gets adjacent to the target's surface, it has enough ionisation



energy to take atoms from the surface (54-55).

Fig 2.3 Schematic diagram describing Sputtering deposition process

(Source - http://clearmetalsinc.com/technology/)

Molecular beam epitaxy (MBE) - Molecular beam epitaxy (MBE) is an alternative PVD process. MBE is an ultrahigh vacuum technology that relies on the controlled evaporation of zinc and the production of ZnO by contact with oxygen gas injected into the chamber. MBE is a technology for the controlled deposition of high quality epitaxial ZnO thin films. MBE provides an accessible method for the doping of ZnO. This is vital to the use of ZnO in advanced electrical devices. It has two major drawbacks: the need for costly substrates for epitaxial deposition of the material (usually sapphire) and the poor deposition rate, which limit the use of MBE-grown ZnO in industry. Nonetheless, it remains an extremely useful research tool for research on high-quality epitaxial ZnO films (56-57).

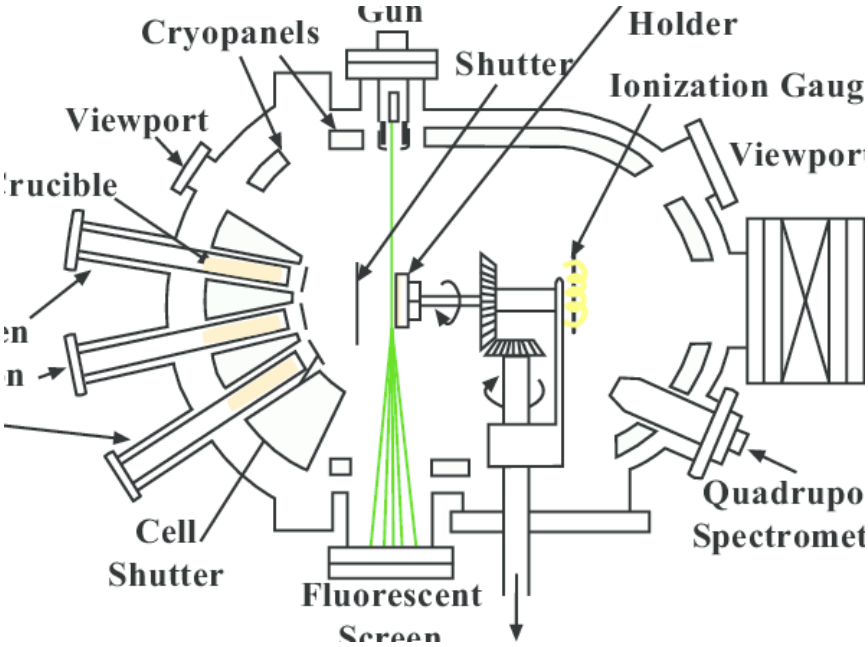


Fig 2.4 Schematic diagram illustrating a Molecular beam epitaxy system.

(Source - https://www.researchgate.net/publication/256143230_Basics_of_Molecular_Beam_Epitaxy_MBE_technique)

Chemical Vapour Deposition (CVD) - Gas phase methods based on chemical vapour deposition (CVD) have been heavily studied for ZnO deposition. A CVD method involves exposing a substrate to a volatile precursor, which then reacts or decomposes on the substrate's surface, resulting in the deposition of the target material. CVD precursors are delivered into a deposition chamber via an inert carrier gas (e.g. nitrogen), and the deposition substrate is held at high temperatures (450°C to 900°C, depending on the procedure).

Instead of employing a ZnO precursor, metal-organic (MO) precursors such as diethylzinc or zinc acetate can be utilised in a technique known as metal-organic chemical vapour deposition (MOCVD). One of the most significant advantages of CVD is that it may be utilised to create 2D morphologies like NWs. This sort of CVD method involves gold-catalyzed growth, in which gold droplets are strategically positioned on the substrate to serve as seeds for NW development. Following the deposition of the gold catalytic structures on the surface, ZnO vapour is injected into the deposition chamber while the substrate is kept at a high temperature (around 850°C). This ZnO interacts with the gold droplet seeds, generating zinc complexes that constitute the foundation for the formation of ZnO NWs (58).

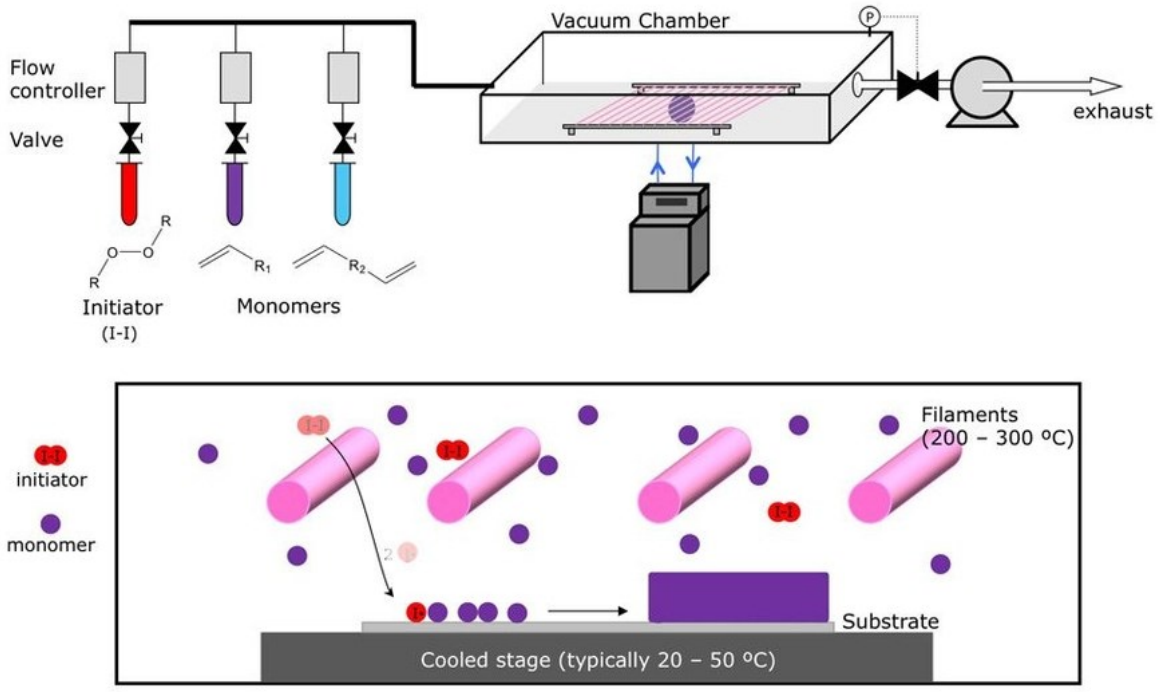


Fig 2.5 a simple diagram representing the Chemical Vapour deposition (CBD) process

(Source - https://news.mit.edu/2015/explained-chemical-vapor-deposition-0619)

Atomic layer deposition (ALD) - Atomic layer deposition (ALD) is a CVD process that involves periodically pulsing and purging zinc oxide precursors. This approach may be used to generate thin films as well as 2D nanostructures (59).

2.1.4.2. Liquid Phase ZnO Growth Methods

Liquid phase methods provide an appealing alternative to gas phase procedures. The sol-gel deposition process is used for developing ZnO thin films with controllable thicknesses. It is based on the creation of a solution containing a zinc precursor, which is subsequently deposited on a substrate using methods such as dip or spin coating. This is one of the approaches employed here to deposit ZnO seed layers for ZnO NW development.

solvothermal synthesis - The most significant and widely used liquid phase zinc oxide growth technique is solvothermal synthesis. Solvothermal growth refers to any procedure in which a material crystallises inside a liquid solution (often water for ZnO, henceforth referred to as hydrothermal synthesis) at high temperature (70°C to 300°C) and high pressure. The growth solution includes the precursors needed to develop the desired substance. To attain the high temperature and requisite high pressure, an autoclave is a Teflon-lined stainless-steel pressure vessel is used. Controlling the temperature, filling, pressure, and concentration of the precursors in the growth fluid allows for a high degree of control over the creation of the desired material. Hydrothermal growth has long been utilised as a high throughput, high quality, and reproducible method for growing bulk crystals of a wide range of materials. The substance resulting from this growth will be either powder or substantial crystals. In the instance of ZnO, hydrothermal growth has been employed to create a wide variety of distinct morphologies such as NWs, hollow spheres, and nanoparticles (60-63).



Fig 2.5 Schematic diagram to present the steps required for Solvothermal synthesis process.

(Source - https://www.researchgate.net/figure/Schematic-diagram-of-solvothermal-synthesis-method_fig1_375771276)

Chemical Bath Deposition (CBD). - In this study, all ZnO NWs were produced on seeded substrates using a hydrothermal growth process called chemical bath deposition (CBD). CBD is a liquid phase approach based on immersing a substrate in the growth solution containing the precursors, such that the growth occurs on the substrate. Unlike hydrothermal growth, the CBD approach requires only a solution container (such as a glass beaker) and a substrate mounting mechanism. This implies that CBD does not require an autoclave because it runs under air pressure (64).

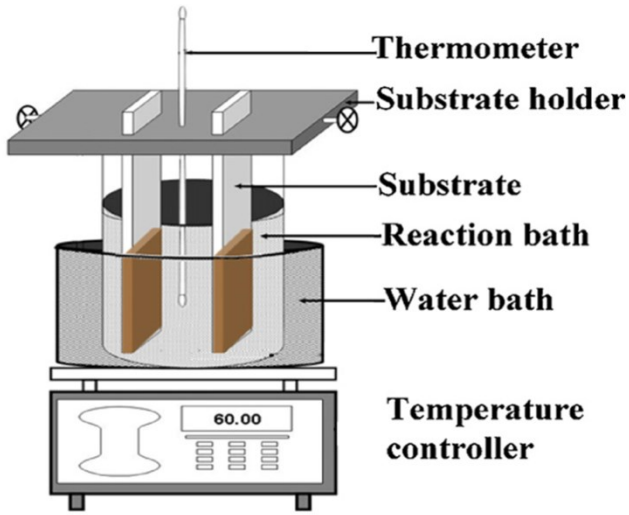


Fig 4.6 A simple schematic diagram representing a setup for Chemical Bath deposition process.

(Source - https://pubs.sciepub.com/jmpc/6/1/2/figure/1)

2.1.4.2.1. Chemical Bath Deposition (CBD)

As this study is based on chemical bath deposition, here is a detail review work on it. CBD The growth of ZnO NWs necessitates the use of an underlying ZnO seed layer to induce NW nucleation, which boosts throughput and quality while also providing control over the NWs' form and orientation.

The CBD process consists of the preparation of an aqueous solution containing the Zn precursor and a reducing agent that supplies hydroxyl radicals to the growth solution. ZnO NWs development requires a Zn2+ precursor as well as a reducing agent. The reaction of these two ions in solution usually yields zinc hydroxide and zinc hydroxide complexes. The hydroxide complexes will combine with water to produce ZnO and more hydroxide radicals, which can then react again. As a result, the first two elements to consider for CBD development in ZnO NWs are Zn2+ and OH- sources. The three most widely utilised zinc precursors are zinc nitrate hexahydrate, zinc acetate dihydrate, and zinc chloride (65-67). Akgum et al. explained in their work that under equivalent growth circumstances, all three salts produce single crystal wurtzite-phase ZnO NWs. A direct comparison of the three zinc salts previously stated is performed while all seed layer deposition and NW development conditions remain unchanged. This study demonstrated that zinc acetate yields greater aspect ratio NWs, followed by zinc nitrate, and lastly zinc chloride (68). Differences in the seed layer deposition, growth temperature, solution pH, and even the vessel in which the growth is done will directly effect NW growth, making it practically hard to construct a full comparison of the influences that zinc salts can have on NW growth.

There are several techniques to supplying the necessary hydroxyl ions in the growth solution for the OH- source. The three primary ways employ distinct chemicals: a strong base such as NaOH or KOH, ammonia hydroxide, or hexamethylenetetramine (HMTA). The first of these three was abandoned owing to the disadvantages of employing a strong base, particularly for future scaling up. To enable the implementation of ZnO NWs in various applications and their potential scale-up. Jung et al. demonstrated the impact of both hydroxyl sources on NW development. In short, both hydroxyl sources can be employed to promote the development of NWs. Their basicity differs, with ammonia hydroxide having a higher

basicity, which will impact NW development due to the effect of growth solution pH on NW growth, mostly due to the increased concentration of OH- (69). Also, according to research of Strano et al., HMTA assures that the single crystal wurtzite phase of ZnO NWs is formed more effectively than other reduction agents. As a result, HMTA was employed in this work (70).

In this work the precursors are specified to zinc nitrate and HMTA. Below written equations are the possible chemical reactions for the chemical deposition process (71).

$$Zn(NO_3)_2 \cdot 6H_2O \rightarrow Zn^{2+} + 2NO^- + 6H_2O \quad \text{[Eq. 2.1]}$$

$$(CH_2)_6N_4 + 6H_2O \rightleftarrows 6HCHO + 4NH_3 \quad \text{[Eq. 2.2]}$$

$$NH_3 + H_2O \rightleftarrows NH^+ + OH^- \quad \text{[Eq. 2.3]}$$

$$(CH_2)_6N_4 + Zn^{2+} \rightarrow [Zn(CH_2)_6N_4]^{2+} \quad \text{[Eq. 2.4]}$$

$$[Zn(CH_2)_6N_4]^{2+} + 2OH^- \rightarrow ZnO + H_2O + (CH_2)_6N_4 \quad \text{[Eq. 2.5]}$$

$$Zn2+ + 4NH^3 \rightarrow [Zn(NH3)4]^{2+} \quad \text{[Eq. 2.6]}$$

$$[Zn(NH3)_4]^{2+} + 2OH^- \rightarrow ZnO + H_2O + 4NH^3 \quad \text{[Eq. 2.7]}$$

$$Zn^{2+} + 4OH^- \rightarrow [Zn(OH)4]^{2-} \quad \text{[Eq. 2.8]}$$

$$[Zn(OH)4]^{2-} \rightarrow ZnO + H_2O + 2OH^- \quad \text{[Eq. 2.9]}$$

The first two equations pertain to the breakdown in water of zinc nitrate hexahydrate (Eq. 2.1) and HMTA (Eq. 2.2). The former offers Zn2+ precursors for the ZnO NWs, whilst the latter decomposes into formaldehyde (HCHO) and ammonia (NH3). This ammonia is

then hydrolysed (Eq. 2.3) into ammonium (NH_4^+) and hydroxyl (OH^-). After that there are three possible reaction pathways towards the formation of ZnO:

i) Zn^{2+} and HMTA may form a complex ion (Eq. 2.4), which is subsequently hydroxylated (Eq. 2.5), yielding water, ZnO, and HMTA. As a consequence, the original HMTA is restored while generating ZnO.

ii) Ammonia from HMTA forms a complex ion with Zn^{2+} (Eq. 2.6), which is then hydroxylated into ZnO, water, and ammonia (Eq. 2.7).

iii) Zn^{2+} creates $[Zn(OH)_4]^{2-}$, a complex hydroxide (Eq. 2.8 & 2.9) that decomposes into ZnO, water, and hydroxyl. This hydroxide complex serves as the foundation for the ZnO NW structure,

As demonstrated by this reaction mechanism, the involvement of HMTA in NW development is critical to completely understanding the growth process and how HMTA concentration affects growth. Because the hydrolysis of HMTA is reversible, the release of OH^- into the growth solution is regulated.

Role Of HMTA In The Nanowire Growth

Strano et al. and Parizes et al. separately demonstrated that The HMTA has two major functions in the evolution of ZnO NW. Regarding the growth responses and processes; First, it functions as a pH modulator, providing the necessary OH^- ions in solution to stimulate growth in a regulated way, comparable to a pH buffer. Second, HMTA adheres to the non-polar lateral faces of the ZnO NWs, causing a steric barrier that restricts the lateral expansion of the NWs because zinc complexes produced in solution cannot access the nonpolar faces of the NWs (70, 72).

Parameters and their influence on the nanowire growth

The precursors employed in this study were zinc nitrate hexahydrate and HMTA. The concentrations employed for each, as well as the ratio between them, must be precisely controlled in order for the ZnO NWs to develop properly. One essential component of the

CBD of ZnO NWs is that as the NWs develop on the seeded substrate, hydrothermal synthesis processes occur in solution, resulting in ZnO nano and microstructures. The growth of these structures in solution consumes the growth precursors at a significantly higher pace than growth on a substrate. As a result, it is critical to ensure that the precursor concentration in the solution is sufficient to sustain NW development for the specified reaction duration. As previously stated HMTA restricts the lateral expansion of NWs while boosting their axial growth and so improving the aspect ratio. However, if the HMTA concentration is too high, it may completely prevent NW development, resulting in the formation of alternative nanostructures such as nanoplatelets or nanodisks. The concentration of zinc nitrate must be sufficient that the NWs can develop under regulated conditions. If the concentration is too high, an unwanted compact ZnO layer will develop; if it is too low, the NWs will not fully form. Regarding the ratios of zinc nitrate and HMTA Strano et al. and Jung et al. thoroughly explained in their work that equimolar ratios provide greater densities of high-quality, high-aspect-ratio NWs. Higher HMTA concentrations than zinc nitrate result in decreased density of higher aspect ratio NWs. These considerations clearly demonstrate that carefully regulating the concentrations of both chemicals is critical for controlling the formation of ZnO NWs (69, 70).

There are three more CBD control factors that directly effect the growth of the NWs: the pH of the growth solution and the temperature and time for CBD growth. Modifying the pH values, for example, by adding a base such as ammonia to the growth fluid, has a significant impact on the shape and size of the as-grown ZnO NWs. Baruah et al. and Verrier et al. had shown that For initial solution growth pH levels in the neutral range (6.3 to 7.3), the CBD procedure produces hexagonal NWs with controlled dimensions. With the rise of pH, the ZnO nanomorphology shifts from NWs to nanoneedles or flower-like structures. Which are undesirable for some applications (73, 74).

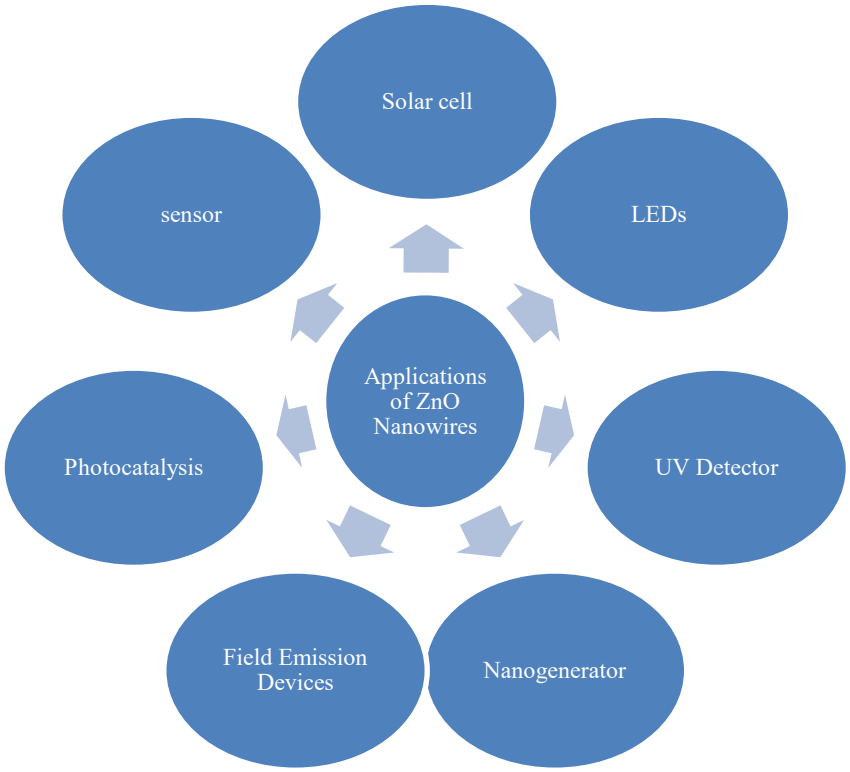
The temperature during growth has a significant impact on the growth kinetics and, consequently, the growth rate of NWs. In summary, higher temperatures increase the kinetics of NW development, resulting in a faster growth rate. However, increasing the temperature has several restrictions. In the case of the CBD method, because the growth occurs in an unsealed processing unit (as opposed to an autoclave in hydrothermal synthesis), the temperature is restricted by the boiling point of the solvent, in this instance water. As a result, the maximum operating temperature ranges between 90°C and 95°C. Temperatures below

90°C, even down to 50°C, will result in NW development, but at a significantly lesser pace. Thus, in this study, 90°C was chosen for all NW growth.

The synthesis growth time is the final CBD growth characteristic mentioned in this article. Its impact on NW development is straightforward: the longer the growing time, the greater the axial and lateral growth. Thus, the synthesis growth time, in conjunction with the precursor concentration, is the primary control parameter for tuning the size of the NWs.

2.1.5. Applications

ZnO nanowires' special electrical, optical, and mechanical qualities make them useful for a



variety of applications across several industries.

Fig 2.3 Various Applications of Zinc Oxide Nanowires

2.1.5.1. Solar cell

Dye-sensitized solar cells (DSSCs), which are composed of oxide semiconductors and organic dyes or metal organic complex dyes, are one of the most promising candidate systems for achieving efficient solar energy because they are more versatile, less costly, and easier to manufacture than silicon solar cells. ZnO-based DSSC technology alternative to TiO2 is regarded one of the most promising materials for solar cells due to quicker electron transport with lower recombination loss, ease of crystallisation, and anisotropic growth (75). Cheng et al. created branched ZnO nanowires on conductive glass substrates using a solvothermal approach for dye-sensitized solar cells. The branched ZnO nanowire DSSCs had a greater short-circuit current density and energy conversion efficiency than the naked ZnO nanowire, with values of 4.27 mA/cm2 and 1.51%, respectively (76). Ko et al. examined different manufactured ZnO nanowire DSSCs with lengthwise (LG) and branched growth (BG). They demonstrated that the total light-conversion efficiency of the branching ZnO nanowire DSSCs was substantially greater than the upstanding ZnO nanowires (77).

2.1.5.2. Light Emitting Diodes (LEDs)

The output power of GaN LEDs with ZnO nanotip arrays can be increased by up to 50 %. A heterojunction LED might be made by growing vertically aligned ZnO nanowires on a p-GaN substrate and using indium tin oxide (ITO)/glass to combine and package (78-80).

2.1.5.3. Ultraviolet Detector

UV detection is another intriguing optical use for ZnO nanowires. The UV detector uses the electric potential of the ZnO nanowires, which changes due to UV irradiation (81-82). Li et al. developed a technique for constructing a ZnO bridging nanowire structure with nanowatt UV detection. The electrodes were produced by thick ZnO layers covering the Au-catalyst-patterned sections on the substrate, and the sensing components were ultralong ZnO nanowires spanning the electrodes. The gadget displayed dramatic fluctuations (10-105

times) in current under a wide range of UV irradiation (10−8-10−2 W cm−2) (83). Chen et al. developed a UV photodetector by connecting a circular spiral ZnO nanowire with 30 nm IrO2 electrodes (82).

2.1.5.4. Nanogenerator

The non-centrosymmetric symmetry of the wurtzite structure causes ZnO to display high piezoelectric behaviour. Nanogenerators (NGs) were created by using the piezoelectric action of ZnO nanowires for scavenging small and irregular mechanical energy such as air flow vibrations and body motions (84-85). Zhu et al. described a flexible high output nanogenerator (HONG) that uses a lateral ZnO nanowire array to capture mechanical energy and power a tiny commercial electronic component (86). Hu et al. applied a nanogenerator to the inner surface of a tire and scavenged mechanical energy from the tire's deformation during travel. The nanogenerator directly powers an LCD panel (87).

2.1.5.5. Field Emission Devices

ZnO nanowires have been explored as potential for field emitters because to their high melting point and good stability in an oxygen environment. Hwang et al. demonstrated vertical ZnO nanowires grown on grapheme/PDMS substrates for transparent and flexible field emission. The ZnO nanowire/graphene hybrids demonstrated exceptional field emission features (88). Chen et al. developed ZnO nanowires using a ZnO:Ga/glass substrate. UV light enhanced the ZnO nanowire field emission and decreased the turn-on electric field (89).

2.1.5.6. Photocatalysis

Zinc oxide nanoparticles (ZnO NPs) have exceptional photocatalytic effects. Sugunan et al. developed a continuous flow water filtration system using ZnO nanowires grown on flexible poly-L-lactide nanofibers. The continuous flow photocatalytic breakdown of organic molecules in water does not need separation of the photochemically active material from the reservoir, and the cleaned water may be collected straight from the reservoir (90). Kuo et al. employed the vapour transport method to create ultralong ZnO nanowires on silicon substrates, which they then used as reusable photocatalysts to degrade rhodamine B and 4-chlorophenol (91).

2.1.5.7. Sensors

One of the most extensively utilised and earliest discovered oxide sensing materials is ZnO.

Gas Sensor

ZnO acts as a gas sensitive material because of its electrical conductivity, which may be significantly altered by the adsorption or desorption of gas molecules on its surface. 1D nanostructured devices, such as nanowires, are more sensitive and selective due to their high aspect ratio and vast surface area. ZnO nanowires can detect several gases, including NO, NO2, CO, NH3, H2, and ethanol (92-97).

Biosensor

ZnO nanostructures have attracted interest in biosensor applications because to several benefits, including nontoxicity, biosafety, biocompatibility, high electron-transfer rates, and conjunction with immobilised enzymes (98). Liu et al. developed an ampere-metric glucose biosensor using aligned ZnO nanorod films produced directly on the surface of ITO glass (99). Choi et al. described a ZnO nanowire field effect transistor (FET)-based biosensor for

detecting low-level biomolecular interactions. With a 7.5 nA current increase, the ZnO nanowire biosensor could detect streptavidin at concentrations as low as 2.5 nM (100).

2.2. SENSOR

A sensor is a device that detects and responds to physical or chemical changes in the environment, transforming them into actionable signals. In more general terms, it might be seen as a module that recognises a quantifiable change in its input, which could be any signal. Sensors may be classified into multiple categories based on their sensing mechanism and output characteristics. The different categories of electrical sensors are Conductometric, Capacitive, Optical, Piezoresistive, Colorimetric, and Electrochemical and so on.

2.2.1. Chemical Sensor

Chemical sensors specifically measure the presence or concentration of chemicals, providing crucial data for applications in healthcare, environmental monitoring, industrial processes, and food safety.

2.2.1.1. Sensor Parameters

A chemical sensor's efficiency is assessed using a number of parameters (101). All of the parameters are detailed below.

Sensitivity - Sensitivity is defined as the change in output in response to a change in input.

Response time - The time it takes for a sensor to achieve 90% of its maximal response against a certain concentration of analyte is known as its response time. Many practical applications require a sensor with a rapid reaction time.

Recovery time - The time it takes for the sensor to return to 10% of its starting condition (base resistance) after sensing a certain concentration of analytes. An efficient sensor should be capable of quickly returning to its initial point.

Response - The sensor response of chemiresistive sensors is defined as the change in electrical behaviour of sensing devices exposed to the analyte. This parameter can be determined in a variety of ways, most often as the ratio of electrical behaviour prior to and following gas exposure based on gas analyte reducing/oxidizing behaviour.

Selectivity - It is often described as the sensor's ability to distinguish an electrical response for a target in the presence of other materials under the same circumstances.

Stability - This parameter takes into account the amount of time the sensor platform will maintain the same electrical response when exposed to a certain analyte under the same conditions.

2.2.2. Heavy Metal Ion Sensor

A heavy metal ion sensor is a chemical sensor used to detect the presence of heavy metal ions in drinking water and ensure compliance with safety requirements. Monitoring and eliminating heavy metals such as Cd (II), Hg (II), Cr (VI), As (V), Cr (III), Cu (II), and Bi

(III) is critical because they accumulate in the food chain and can infiltrate living systems via food and drinking water. Heavy metal ion sensors are classified into several categories, including optical, electrochemical, and semiconducting materials-based sensors. Optical methods give precise readings, but are expensive, need experienced specialists to use, and are large, restricting their everyday use. Electrochemical sensors, on the other hand, use liquid electrolytes, making them unsuitable for regular heavy metal ion detection by the general population. Their use demands adequate training and experience from competent specialists (102-107).

2.3. HEAVY METALS

Heavy metals are commonly referred to as a group of metals and metalloids. These elements possess relatively high densities, atomic weights, and atomic numbers. The density ranges from 3.5 g/cm3 to more than 7 g/cm3. The phrase "heavy metal" originally originated in 1817, when German chemist Leopold Gmelin divided the elements into three categories: nonmetals, light metals, and heavy metals. Common heavy metals include lead, mercury, cadmium, chromium, and arsenic. These metals are widely distributed in the environment as a result of natural events such as volcanic eruptions and human activities such as mining, industrial production, and agricultural usage. While some heavy metals are required in tiny levels for biological activities, prolonged exposure can result in serious health consequences.

Lead and mercury, for example, are neurotoxins that can harm the brain and neurological system, especially in youngsters. Cadmium exposure has been associated to kidney disease and bone demineralisation, whereas arsenic and chromium are proven carcinogens. Heavy metals' persistence and bioaccumulation in ecosystems make them a major environmental issue, since they may pollute soil, water, and food sources, raising long-term threats to human health and the environment (108-111).

2.3.1. Copper (Cu)

Copper can be found in the environment in three forms: metallic (Cu0), cuprous (Cu+), and cupric (Cu2+).Copper is an extremely hazardous metal in high amounts in water. However, a trace quantity of copper is required for enzyme production and bone growth in humans. Major sources of copper include metallurgy and mining industries, steel industries, chemical manufacture, paints, fertilisers, and electroplating. Copper can be harmful because of the Cu2+-Cu+ transition, which produces superoxide and hydroxyl radicals. Excessive copper consumption can cause cellular damage and lead to illnesses including Wilson's disease, Alzheimer's disease, Parkinson's disease, and even death (112-114).

2.3.2. Chromium (Cr)

Chromium (Cr) is the seventh most prevalent element on Earth, and it occurs naturally in various oxidation or valence states in the earth's crust. Chromium ions are available in a spectrum of forms, with Cr3+ being the most stable and Cr6+ being the second most stable [55]. The primary sources of chromium in water are the metallurgical, refractory, and chemical sectors. however, Cr6+ compounds have been linked to a variety of health concerns, including inflammation, stomach and small intestine ulcers, anaemia, sperm destruction, and male reproductive system impairment. Individuals exposed to Cr6+ by drinking water have also been found to have an increased risk of developing stomach tumours (115-117).

2.3.3. Iron (Fe)

Iron (Fe) hardly categorised as a heavy metal in the traditional sense because it is a necessary element for many biological processes in humans and animals. Iron, as a constituent of haemoglobin and certain enzymes, is essential for oxygen transport, DNA synthesis, and energy generation. However, in large quantities, iron may be poisonous and

cause health hazards. Elevated iron levels, such as those found in hemochromatosis or from environmental pollution, can cause oxidative stress and organ damage, including the liver, heart, and pancreas. Unlike many other heavy metals, iron toxicity is caused mostly by metabolic problems or excessive supplementing, rather than ambient exposure (118).

2.3.4. Nickel (Ni)

Nickel (Ni) is classified as a heavy metal and is widely utilised in a variety of industrial applications, including stainless steel manufacture, batteries, and electroplating. While nickel is a necessary trace metal for some species, excessive exposure causes serious health concerns to both humans and the environment. Inhaling or consuming excessive doses of nickel can result in lung problems, skin rashes, and other allergic responses. Long-term exposure to nickel compounds, particularly in industrial settings, is related with an increased risk of lung and nose malignancies due to their carcinogenic qualities. Nickel pollution can also develop in water and soil due to mining, refining, and waste disposal operations. Nickel may be hazardous to plants and aquatic species at high quantities, causing ecological and food chain disruptions (111, 119).

Chapter-3:

METHODOLOGY

3. METHODOLOGY

In this section, the experimental process of the device fabrication is explained, as well as different characterization processes such as X-Ray Diffraction (XRD), Diffuse Reflectance Spectroscopy (DRS), Field Emission Scanning Electron Microscope (FESEM), and current-voltage characteristic are included. Also the detection processes of few selected Heavy metals are provided.

3.1. FABRICATION

3.1.1 Materials and the Instruments

Chemicals used in the fabrication procedure are-

I. Zinc Nitrate Hexahydrate : $Zn(NO_3)_2.6H_2O$ [Molecular Weight-297.49] (Sigma-Aldrich)
II. 25% Ammonia Solution : NH_4OH[Molecular Weight-35.05] (Sigma-Aldrich)
III. Hexamethylenetetramine (HMTA) : $C_6H_{12}N_4$ [Molecular Weight-140.19] (Sigma-Aldrich)
IV. p-type Silicon (100) wafer (Ted Palla)

The Instruments involved in the fabrication procedure are-

I. Magnetic Stirrer with Hot Plate
II. Regulated DC Power Supply
III. Hot Air Oven

3.1.2 ZnO Growth Process

In this work, a double chemical bath Deposition (CBD) process is used, where the first CBD provide the seed layer on the substrate and the second CBD controls the further growth of the ZnO. Also to gain certain morphology of ZnO the entire CBD process was under voltage control so it can be said that this is a Voltage –assisted CBD method. p-type Silicon (100) wafer was utilised as a substrate.

3.1.2.1. Substrate Preparation

Initially, Piranha Solution was produced. 6mL of sulphuric acid (H2SO4) was slowly poured into 6mL of hydrogen peroxide (H2O2) to create a 1:1 solution of H2SO4 and H2O2. This is a very exothermic process. The solution was employed to continue proceedings until the situation calmed down. The wafers were then immersed in the Piranha Solution for an hour, or until the effervescence subsided. Following that, the wafers were withdrawn from the solution and washed with De-ionized Water (DI Water) to eliminate any Piranha residue.

A 1:10 solution of Hydrofluoric Acid (HF) in DI water was prepared. The wafers were put into it to remove any oxide from the surface. The wafers remained in the solution for roughly a minute. Finally, the wafers were withdrawn from the solution, washed with DI water, and allowed to dry.

Silver Paste was applied to both sides of the p-Si (100) substrate and heated in the Hot Air Oven for 1 hour at 150°C. Natural cooling within the Hot Air Oven takes around 1.5-2 hours. This Silver Paste deposition was performed to create a metal contact with the wires that would be linked to the positive and negative ports of the Regulated DC Power Supply while executing voltage-assisted growth of Zinc Oxide Nanowire over the p-Si (100) substrate. The substrate was ready for further experimentation.

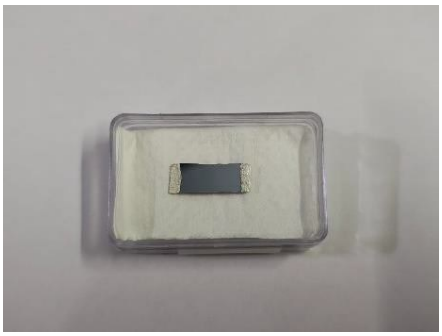
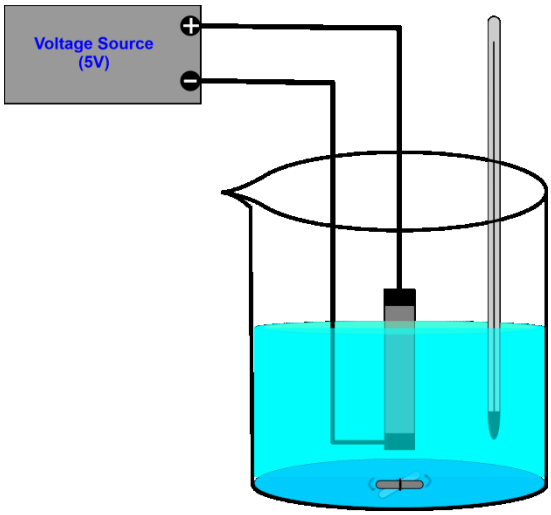


Fig 3.1: A Silver Paste deposited p-Si (100) substrate

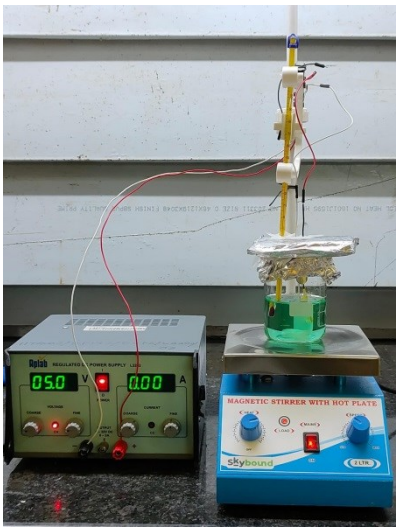
3.1.2.2. Double Step Chemical Bath Deposition (CBD) Method for Synthesis of ZnO Nanowire:

The following two processes describe the growth of ZnO nanowires on the p-Si (100) substrate:

i. Step 1: ZnO Seed Layer Deposition
ii. Step 2: ZnO nanowire development.



(A)



(B)

Fig3.2 (A) Simple schematic diagram of the Voltage-Assisted Chemical Bath Deposition (CBD) method

(B) Experimental Setup for the Voltage-Assisted Chemical Bath Deposition (CBD) method

Step 1: ZnO Seed Layer Deposition

The ZnO seed layer growth procedure begins with the preparation of a precursor solution containing 5mM Zinc Nitrate Hexahydrate [Zn(NO3)2.6H2O] dissolved in 100mL DI water. The precursor solution was agitated at 120 rpm, and the temperature was allowed to rise to 60°C. The sample was vertically inserted into the precursor solution such that the negative terminal dipped into the solution while the positive terminal remained outside with the help of a continuous DC bias, as shown in Figure 3.2A. After reaching the desired temperature, 8mL of 25% ammonia is added to the solution, and the colour changes to milky white. This process was performed for 30 minutes, with the solution temperature held constant at 90°C (±5°) for the nucleation of the ZnO seed layer. Once the nucleation was complete, the ZnO seed layer deposited p-Si (100) substrate was removed from the solution and immersed in DI water for cleaning the precipitations.

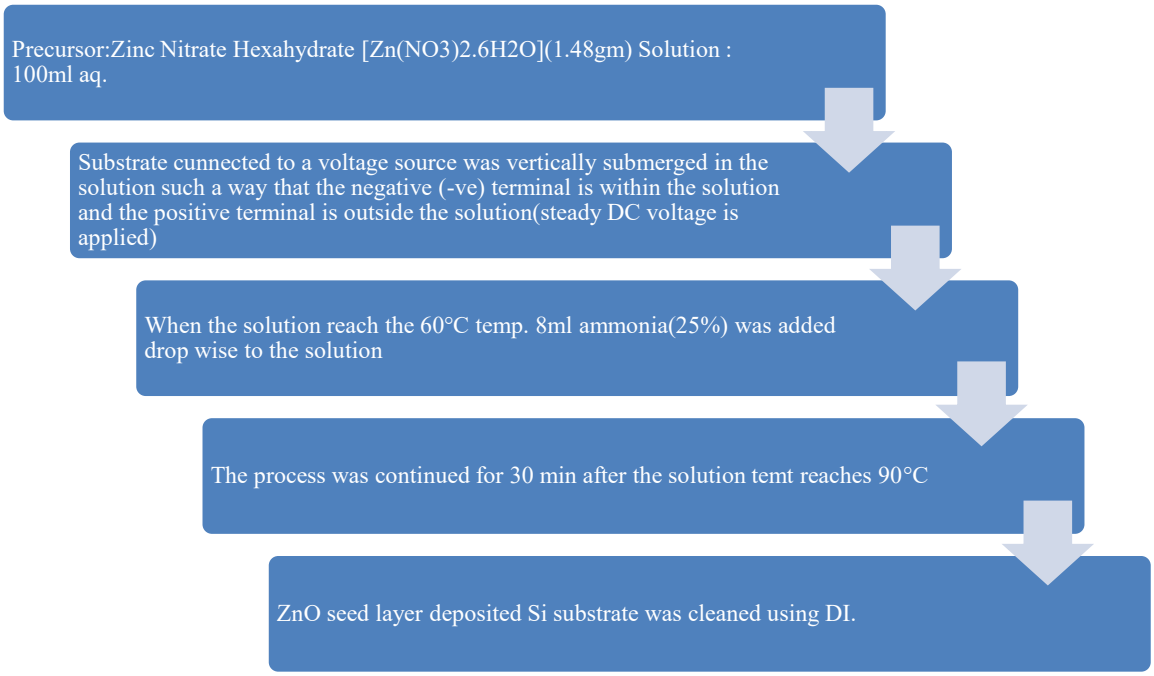


Fig 3.3 Flow Diagram of The ZnO seed layer growth procedure

Step 2: ZnO nanowire development

The development of ZnO Nanowire was accomplished by dissolving 2.5mM Zinc Nitrate Hexahydrate [Zn(NO3)2.6H2O] in 50 mL DI water. Another solution was made separately by dissolving 2.5mM Hexamethylenetetramine (HMTA) in 50 mL DI water. Both solutions were blended together and a ZnO seed layer generated p-Si (100) substrate was put vertically into the solution using a similar arrangement, with the help of a continuous DC bias. The solution was heated to 90 °C to create Zn2+ and OH− ions, initiating the formation of ZnO nanowires. To develop the ZnO nanowires, the deposition was carried out for two hours. The possible chemical reactions which were associated with the growth of ZnO Nanowires are already discussed at section 2.1.4.2.1

$$Zn(NO_3)_2 \cdot 6H_2O \rightarrow Zn^{2+} + 2NO^- + 6H_2O \quad \text{[Eq. 3.1]}$$

$$(CH_2)_6N_4 + 6H_2O \rightleftarrows 6HCHO + 4NH_3 \quad \text{[Eq. 3.2]}$$

$$NH_3 + H_2O \rightleftarrows NH^+ + OH^- \quad \text{[Eq. 3.3]}$$

$$(CH_2)_6N_4 + Zn^{2+} \rightarrow [Zn(CH_2)_6N_4]^{2+} \quad \text{[Eq. 3.4]}$$

$$[Zn(CH_2)_6N_4]^{2+} + 2OH^- \rightarrow ZnO + H_2O + (CH_2)_6N_4 \quad \text{[Eq. 3.5]}$$

$$Zn2+ + 4NH^3 \rightarrow [Zn(NH3)4]^{2+} \quad \text{[Eq. 3.6]}$$

$$[Zn(NH3)_4]^{2+} + 2OH^- \rightarrow ZnO + H_2O + 4NH^3 \quad \text{[Eq. 3.7]}$$

$$Zn^{2+} + 4OH^- \rightarrow [Zn(OH)4]^{2-} \quad \text{[Eq. 3.8]}$$

$$[Zn(OH)4]^{2-} \rightarrow ZnO + H_2O + 2OH^- \quad \text{[Eq. 3.9]}$$

The initial step of HMTA hydration happens at 60 °C, yielding Formaldehyde (CH2O), which evaporates instantly. Another result of this process is ammonia (NH3), which supports the production of the ammonium cation NH4+ by NH3 protonation. These reactions progressively liberate OH- ions from the precursor solution. Zn2+ ions combine with NH3 to form tetraamine zinc species. $Zn(NH_3)_4^{2+}$ undergoes a reaction with hydroxyl ions to generate Zn(OH)42−, which is more stable than amine complexes. NH4(NO3) is subsequently formed to keep the aqueous solution's pH level stable under supersaturating conditions. Zn2+ ions react with OH− ions in solution, forming zinc complexes. [Zn(OH)4]Thermal decomposition of 2− ions leads to the nucleation of wurtzite ZnO by self-orientation. The electric field applied during growth controls the kinematics of Zn2+ and OH ions near substrate surfaces.

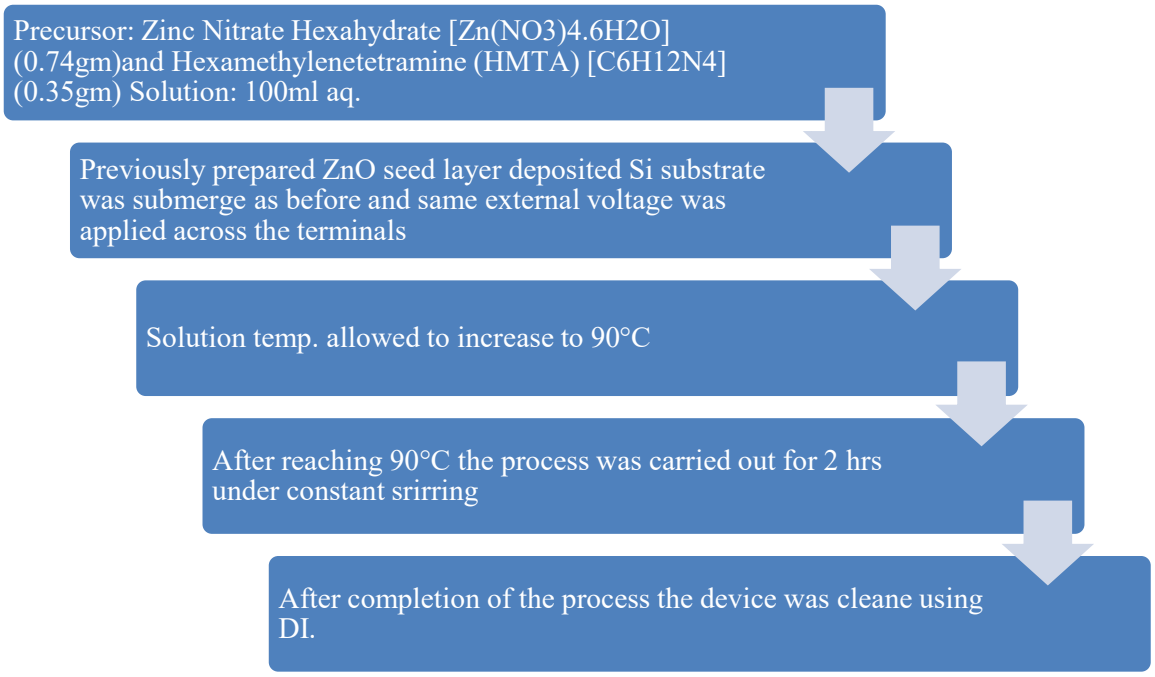


Fig 3.4 Flow diagram of the Step 2: ZnO nanowire development

During the process, the presence of a constant applied voltage caused more Zn2+ ions to collect towards the negative terminal and less Zn2+ ions to accumulate towards the positive terminal. This ion concentration gradient may affect the shape of the produced ZnO. As a result of the presence of Zn2+ ions at the negative terminal, there is a potential of lateral nanowire development.

3.1.2.3 Variation in Growth Parameter

If the growth parameters are changes then different devices can be fabricated featuring different characteristics. Here only the applied external voltage are changed keeping other parameters such as Temperature, Duration, and pH same for Four Devices. So four devices are fabricated keeping all parameters same and just changing the external voltages to 2.5V, 5.0V, 7.5, and 10.0V. For further discussion about these four devices they are named as SET 1(V2.5), SET 2(V5.0), SET 3(V7.5), and SET 4(V10.0).

NAME	STEP 1				STEP 2			
	TEMP. (°C)	DURATION (MIN)	pH (NH3 controlled)	EXT. VILTAGE(V)	TEMP. (°C)	DURATION (Hrs)	pH (HMTA controlled)	EXT. VILTAGE(V)
SET 1 (V2.5)	90°C	30 MIN	same	2.5V	90°C	2 Hrs	same	2.5V
SET 2 (V5.0)	90°C	30 MIN	same	5.0V	90°C	2 Hrs	same	5.0V
SET 3 (V7.5)	90°C	30 MIN	same	7.5V	90°C	2 Hrs	same	7.5V
SET 4 (V10.0)	90°C	30 MIN	same	10.0V	90°C	2 Hrs	same	10.0V

Table 3.1 Variation in growth parameters during fabrication process

3.2 CHARACTERIZATION

3.2.1 X-Ray Diffraction (XRD)

X-Ray Diffraction (XRD) was performed on BRUKER D8 ADVANCE to study the crystallographic nature of those four devices (i.e. SET 1(V2.5), SET 2(V5.0), SET 3(V7.5), and SET 4(V10.0).). The XRD source was Cu kα having $\lambda_{avg.}$ = 1.5418 Å; the scan was done with 2θ range of 30° to 70° with a scan rate of 1°/min.. Then the data was analysed using software "origin pro". Then the results were further analysed to get the crystallite sixe of each devices.

The XRD pattern was analysed to get the crystallite size of the synthesized ZnO nanowires. The Scherrer's equation was used to get the crystallite size related to each plane ZnO shown in the XRD pattern. Also Williamson-Hall plot was utilised to get the crystallite size for each devises.

$$\mathbf{D = \frac{k\lambda}{\beta cos\theta}}$$ (Equation 3.1)

equation 3.1 represents the Scherrer's equation D is the crystallite sizes, where k is the correlation factor (0.89), the λ is the used X-ray wavelength (1.5418 Å), β is the full width at half-maximum (FWHM) of a peak and θ is Bragg's diffraction angle (108).

On the other hand, the Williamson-Hall plot can be drawn using the following equation ,

$$\boldsymbol{\beta_{(hkl)} cos\theta = \frac{k\lambda}{D} + 4\sigma sin\theta} \qquad \text{(Equation 3.2)}$$

Where,

$\beta_{(hkl)}$ = full width at half-maximum of the peak of specific plane

θ = Bragg's diffraction angle

k= correlation factor

λ =X-ray wavelength

D= crystallite sizes

σ = strain

From the above mention equation, a table of points are prepared where $\beta_{(hkl)}\cos\theta$ as y-axis and $\sin\theta$ as x axis. If these points are plotted then a point distribution can be seen. When those points are fitted in a straight line, it gives a y intercept and slope. Where the y intercept represent $k\lambda/D$, thus the crystallite size can be calculated and the slope represents the σ or strain, here a positive slope represent ensile strain and negative lope represents compressing strain.

3.2.2 Diffuse Reflectance Spectroscopy (DRS)

Diffuse Reflectance Spectroscopy (DRS) was used to analyse the optical properties of those devices. As there was a definite variation in growth at the ends due to the applied external bias, the devices were split into 2 parts to get better characteristics data. Let name them for so that data analysis became easier, SET 1(nV2.5), SET 2(nV5.0), SET 3(nV7.5), and SET 4(nV10.0) SET 1(pV2.5), SET 2(pV5.0), SET 3(pV7.5), and SET 4(pV10.0) . The "n" and 'p' are denoted because

those ends were near the negative and positive terminal simultaneously during the fabrication process.

The scan was performed in the range of 200nm to 800 nm with the step size of 1nm and duration of 20 min.. The data were analysed in software "Origin pro".

For analysing the optical properties of a material, energy bandgap can be calculated from absorbance /reflectance spectra. With the help of Tauc plot the energy bandgap can be calculated.

The Tauc approach assumes that the energy-dependent absorption coefficient α may be represented using the following equation.

$$(\alpha . h\nu)^{1/\gamma} = B(h\nu - Eg) \qquad \text{(Equation 3.3)}$$

Where,

α = absorption coefficient

h= Planck constant

ν= Photon Frequency

γ= Factor (1/2 for direct and 2 for indirect transition)

Eg= Energy bandgap

This equation is use to determine the bandgap from absorbance spectra (116).

The energy bandgap also can be calculated from reflectance spectra.
P. Kubelka and F. Munk in their theory explained how the reflectance spectra can be transformed to the corresponding absorption spectra (117).
The conversation is calculated using Kubelka-Munk Function.

$$F(R_\infty).h\nu = \frac{K}{S} = \frac{(1-R_\infty)^2}{2R_\infty} \qquad \text{(Equation 3.4)}$$

Where,
K= absorption coefficient
S=scattering coefficient
$R_\infty = R_{sample}/R_{standard}$= Reflectance of infinity thick specimen
By replacing the α (absorption coefficient) with the Kubelka-Munk function $F(R_\infty)$ in the Tauc method the bandgap can be calculed.

$$(F(R_\infty).h\nu)^{1/\gamma} = B(h\nu - Eg) \qquad \text{(Equation 3.5)}$$

The plot was drawn using this this equation, where the $(F(R_\infty).h\nu)^2$ as y-axis and hν as x-axis.

3.2.3 Field Emission Scanning Electron Microscope (FESEM)

Field Emission Scanning Electron Microscope (FESEM) was per formed on "ZEISS MERLIN COMPACT" having resolution of 0.8nm 0.15KV to study the morphology of the device. The device SET 2(V5.0) was scanned to get the morphological data. The device was split into two part SET 2(nV5.0) and SET 2(pV5.0) to get morphological data of both ends.

3.2.4 Current-Voltage Characteristic

Current-Voltage Characteristic was measured to get the electrical properties of the devices. The I-V Characteristics were measured using "KEITH Source and Measurement Unit (SMU)", within the range of -10V to +10V.

Equivalent Circuit

To get a comprehensive understanding of the devices, an equivalent circuit was drawn using the software "Pspice Student." So the I-V characteristics of the actual devices match those of the equivalent circuit.

3.3 HEAVY METAL DETECTION

In this work, a few specific heavy metal ions are used to test the fabricated devices. It was done to observe the devices' electrical response in presence of those heavy metal ions, so the devices can be used as Chemiresistive heavy metal sensors. The comprehensive data was collected using a "Probe Station", where the I-V characteristics of those devices (i.e. SET 1(V2.5), SET 2(V5.0), SET 3(V7.5), and SET 4(V10.0)) were measured within the range of 0V to +10V in the presence of different heavy metal ions.

As-prepared 100ppm stock solution of Cu(II), Cr(III), Fe(III) and Ni(II) were used as target heavy metal ions to characterise the devices in their presence. After device was set to the probe station such a way that 2 probe is at contact with both end as a 2 terminal device, then as-prepared stock solution was added on the device (dropwise). After every detection process the device was thoroughly washed using DI (Deionized Water).

Chapter-4:

RESULTS AND DISCUSSIONS

4. RESULTS AND DISCUSSIONS

In this section, the data obtained from different characterisation methods such as XRD, DRS, FESEM, I-V Characteristics were analyse and discussed in details.

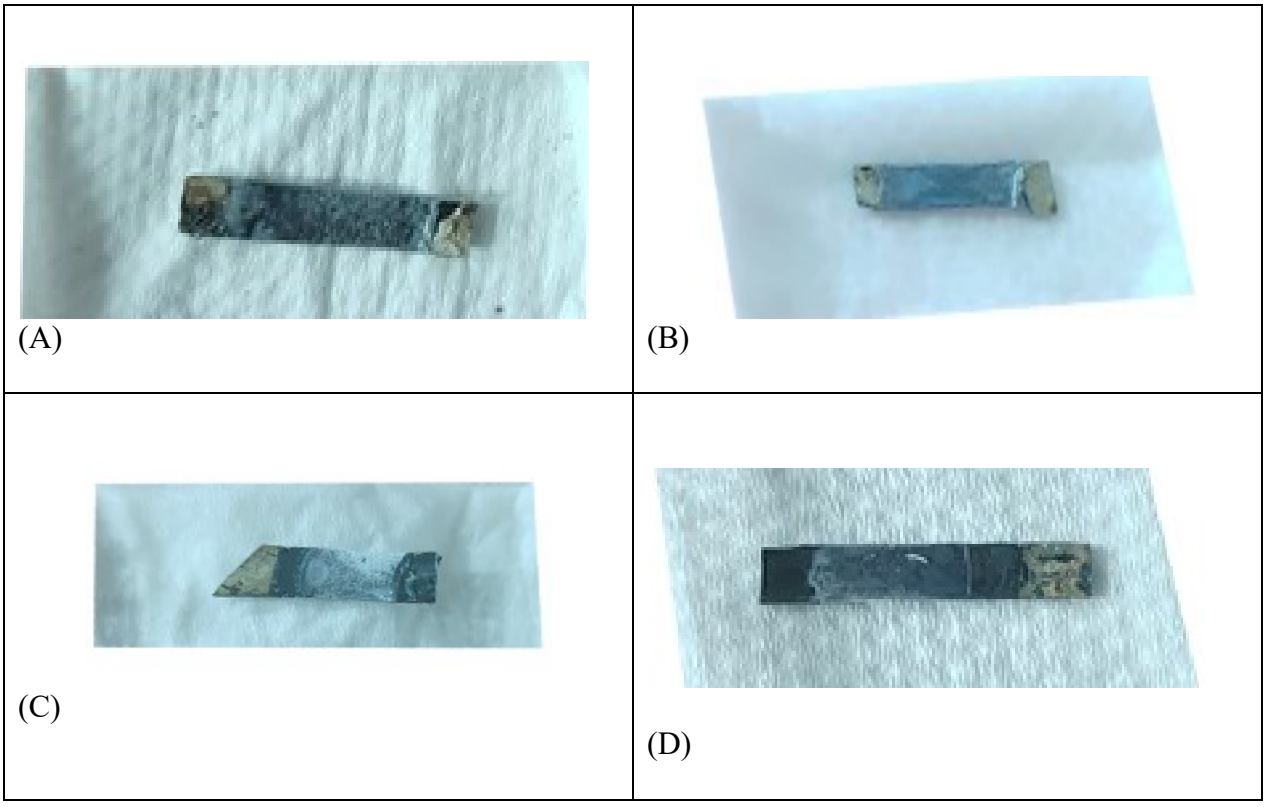


Fig 4.1 The Devices fabricated using Voltage-assisted double chemical Bath Deposition.

(B) SET 1(V2.5); (B) SET 2(V5.0); (C) SET 3(V7.5); (D) SET 4(V10.0)

The thickness of the Silicon substrate - 525µm

The thickness of the device after the fabrication - 547µm

4.1. Structural And Morphological Properties

4.1.1. X Ray Diffraction (XRD) Analysis

X-ray diffraction was utilised to analyse the ZnO nanowire grown on the p-Si substrate using chemical bath deposition. As the growth condition was changed (i.e., different applied voltage), there could be a possibility of different crystallinity for those 4 devices.

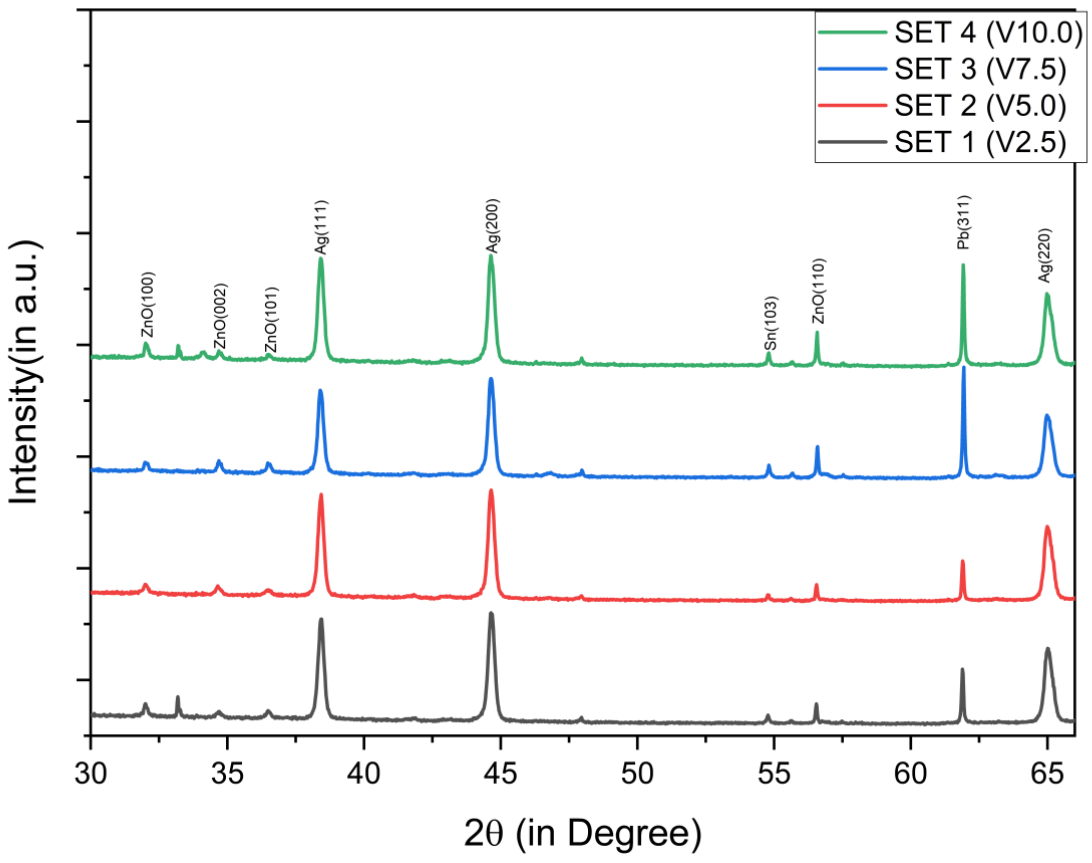


Fig 4.2 XRD pattern of the ZnO Nanowire grown on Silicon Substrate using Voltage-Assisted Chemical Bath Deposition (CBD). SET 1(V2.5), SET 2(V5.0), SET 3(V7.5), and SET 4(V10.0) are the 4 fabricated devices

The XRD pattern shown in Fig 4.2 present the diffraction pattern for those four devices fabricated using different applied voltage during CBD method. It is quite clear that those four devices has peak position at same 2θ value. It is possible to identify all materials present in the device from the XRD pattern. The peaks present in this pattern are 32.06°, 34.68°, 36.47°, 38.42°, 44.63°, 54.88°, 56.58°, 61.91°, and 64.97°. These angles are associated with different planes of ZnO, Ag, Pb and Sn. The table below present the angle and the plane associated with those angles. The peaks are matched with The Joint Committee on Powder Diffraction Standards (JCPDS) -International Centre for Diffraction Data (ICDD)

. The JCPDS-ICDD file no. 36-1451 - Zinc oxide (ZnO),

JCPDS-ICDD file no. 04-0783 - Silver (Ag)

JCPDS-ICDD file no.23-345 - Lead(Pb)

JCPDS-ICDD file no. 19-1365 - Tin(Sn)

NO	2θ	Materials and Planes
1	32.06°	ZnO(100)
2	34.68°	ZnO(002)
3	36.47°	ZnO(101)
4	38.42°	Ag(111)
5	44.63°	Ag(200)
6	54.88°	Sn(103)
7	56.58°	ZnO(110)
8	61.91°	Pb(311)
9	64.97°	Ag(220)

Table 4.1 List of peaks found in XRD pattern and the materials and planes associated with them

As shown in the Table4.1, there are 4 distinctive peak corresponds to the planes (100), (002), (101), and (103) of ZnO wurtzite structure. The presence of Silver also can be seen in this XRD result. As the both side of the devices was coated with silver paste for contact, that silver may be the reason of those peaks. Also presence of Lead (Pb) and Tin (Sn) can be seen. It can be explain by the presence of soldering wire, which are the alloy of lead and tin. Their presence in XRD pattern can be due to the some Soldering wire residue left on the dried silver paste which was used to attach the wire.

Crystallite size

The XRD results were also used to analyse the crystallite size of the ZnO Nanowire.

	2θ	Planes	Crystallite Size	
			Scherrer's Equation(nm)	W-H Plot(nm)
SET 1(V2.5)	32.00°	ZnO(100)	8.613543115	3.988145294
	34.70°	ZnO(002)	6.258614243	
	36.49°	ZnO(101)	6.805904847	
	56.54°	ZnO(110)	16.2891015	
SET 2(V5.0)	32.00°	ZnO(100)	7.626048678	3.499099447
	34.65°	ZnO(002)	6.469403056	
	36.52°	ZnO(101)	5.143553743	
	56.55°	ZnO(110)	15.56923722	
SET 3(V7.5)	31.98°	ZnO(100)	7.65073627	4.346094101
	34.69°	ZnO(002)	8.221738838	
	36.48°	ZnO(101)	7.02176643	
	56.59°	ZnO(110)	15.40645599	
SET 4(V10.0)	32.0°	ZnO(100)	9.263425577	4.690113589
	34.69°	ZnO(002)	8.899258777	
	36.48°	ZnO(101)	6.609732885	
	56.57°	ZnO(110)	17.34730773	

Table 4.2 Comparison of Crystalline size using Scherrer's Equation and Williamson-Hall Plot

To farther analyse the XRD data the Scherrer's Equation and Williamson-Hall plot was used to calculate the crystallite size of the ZnO nanowires.

According to the Scherrer's Equation the crystallite size can be calculated from peak position and the Full Width at Half Maxima (FWHM).

$$D = \frac{k\lambda}{\beta cos\theta} \qquad \text{Equation 4.1}$$

D is the crystallite sizes

k is the correlation factor (0.89)

λ is X-ray wavelength (1.5418 Å)

β is the full width at half-maximum (FWHM) of a peak

θ is Bragg's diffraction angle

From Table 4.2 , it can be seen that the four device have almost same crystallite size for each plane . Also the ZnO(100), ZnO(002) and ZnO(101) have almost same crystallite size but ZnO(110) is greater than others.

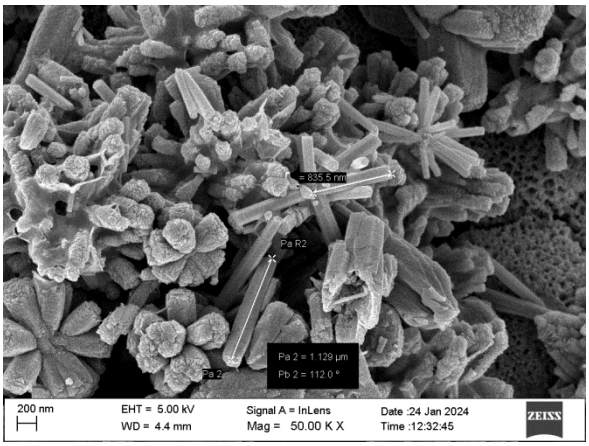
The Williamson-Hall plot can be used to analyse the crystallite size of a material from its XRD pattern. The following formula is used to calculate this.

$$\beta cos\theta = \frac{k\lambda}{D} + 4\sigma sin\theta \qquad \text{Equation 4.2}$$

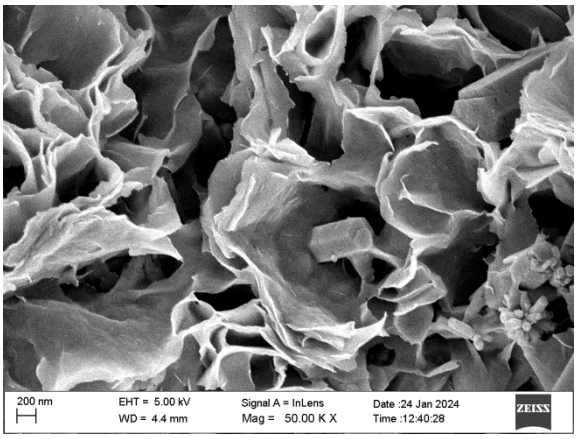
As previously mentioned the β is the full width at half-maximum of the peak of specific plane, θ is Bragg's diffraction angle, correlation factor is k, λ is the used X-ray wavelength, crystallite sizes D and σ is strain. By plotting the βcosθ as Y-axis and sinθ as x-axis a point distribution was plotted for all those peaks. When those points were linear fitted in straight line, their slope and intercept were σ and kλ/D respectively. Their values were provided in the Table 4.2

4.1.2. Field Emission Scanning Electron Microscopy (FESEM) image Analysis

In this work, the aim was to get a different morphology of ZnO nanowire by applying external voltage during the Chemical Bath Deposition process. To get a better understanding of that effect Field Emission Scanning Electron Microscopy was done on a device (SET 2(V5.0)). As it was expected to get different morphology at each end, thus that device was split into two part SET 2(pV5.0) and SET 2(nV5.0).



(A)



(B)

Fig 4.3 the FESEM image of the device SET 2 (V5.0). (A) image of the section SET 2 (pV5.0) (B) image of the section SET 2 (nV5.0)

As targeted in this work, a steady voltage was applied during the CBD process and the negative terminal was dipped within the precursor solution. As previously explained in section 3.1.2.2 that the ZnO growth is controlled by complex $[(OH)4]^{2-}$ tetrahydroxozincate(II) ion which then turn into ZnO . The formation of this complex depends upon the Zn2+ concentration, so with higher concentration of Zn2+ lead to higher growth rate.

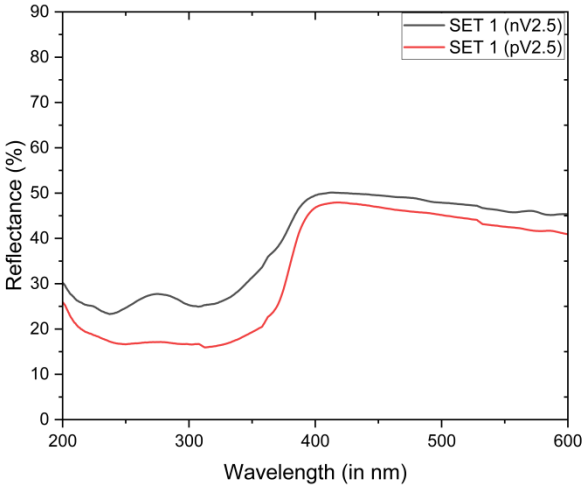
As clearly visible in the FESEM images, there are 2 distinct morphologies at the end of the devices. The devices connected to the positive terminal shows the rod like structure and the other end which was connected to negative terminal has Flake-like structure. So it can be said for the formation of the flake like structure there were higher lateral growth during the CBD process. As this end was connected to the negative terminal which attract the Zn2+ ion

thus has higher concentration relative to the other end during the growth process. This leads to this difference in morphologies.

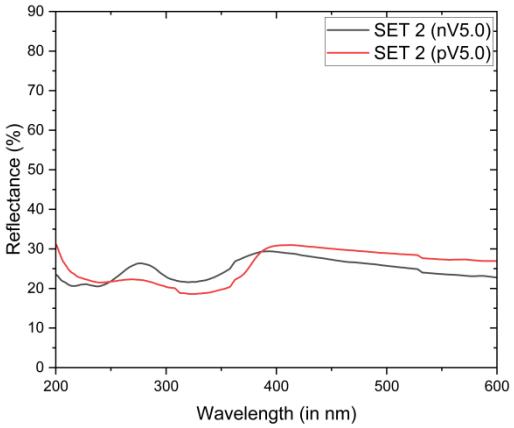
4.2. Optical Properties

4.2.1. Diffuse Reflectance Spectroscopy (DRS) analysis

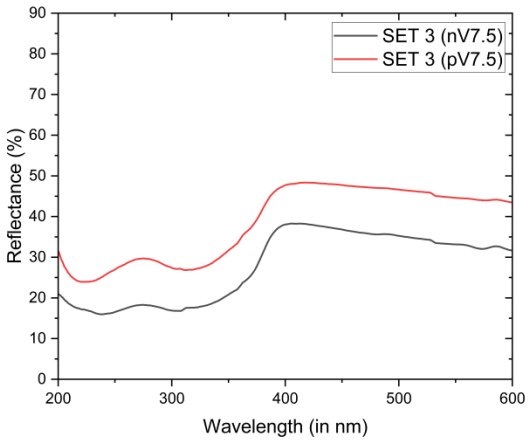
Diffuse reflectance spectroscopy (DRS) was used to analyse the effect of difference in fabrication method on the reflectance of the devices.



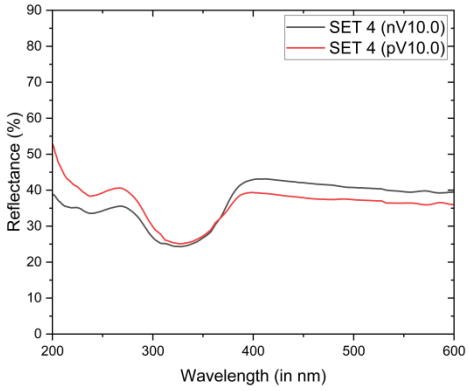
(A)



(B)



(C)



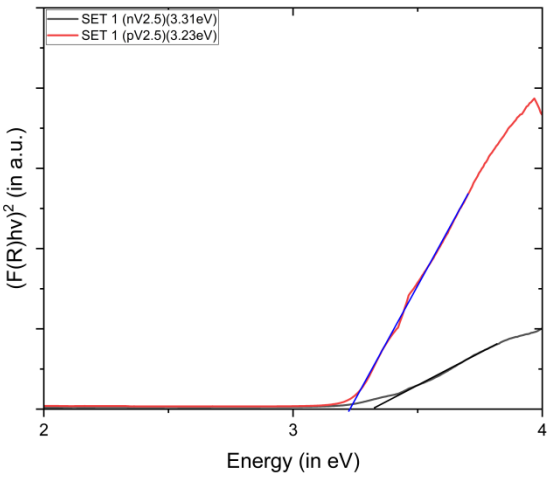
(D)

Fig 4.4 Reflectance spectra of the devices

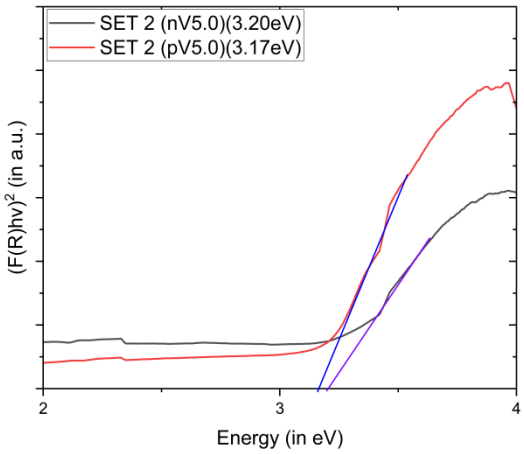
(B) SET 1(V2.5); (B) SET 2(V5.0); (C) SET 3(V7.5); (D) SET 4(V10.0)

As the devices were split into two parts to get a better understanding of the effect of applied voltage during the CBD process, different data was collected for them. In Fig 4.4 shows that there are distinctive differences in reflectance for the both ends for each device.

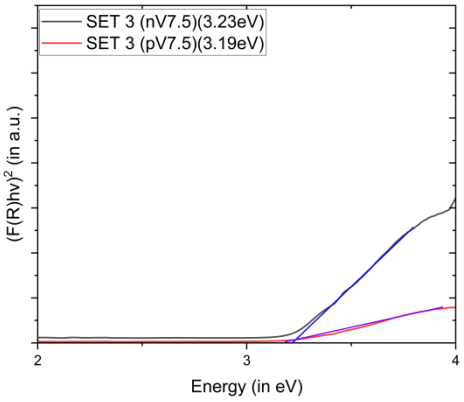
The bandgaps were calculated using these reflectance spectra to get optical bandgap of the devices.



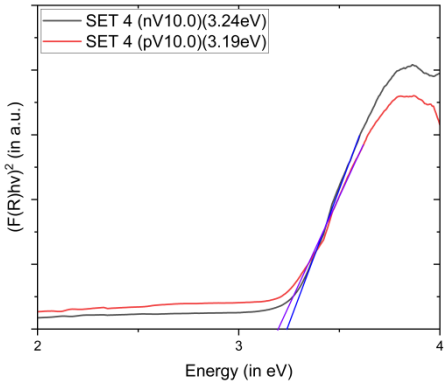
(A)



(B)



(C)



(D)

Fig 4.5 Bandgap energy (Eg) calculation from Tauc plot for determining the bandgap energy of both ends of the devices

(A) SET 1(V2.5); (B) SET 2(V5.0); (C) SET 3(V7.5); (D) SET 4(V10.0)

Device	Sections	Bandgap Energy(Eg)(eV)
SET 1(V2.5)	SET 1(nV2.5)	3.31
	SET 1(pV2.5)	3.23
SET 2(V5.0)	SET 2(nV5.0)	3.20
	SET 2(pV5.0)	3.17
SET 3(V7.5)	SET 3(nV7.5)	3.23
	SET 3(pV7.5)	3.19
SET 4(V10.0)	SET 4(nV10.0)	3.24
	SET 4(pV10.0)	3.19

Table 4.3 Bandgap energy (Eg) calculation from Tauc plot for determining the bandgap energy of both ends of the devices SET 1(V2.5), SET 2(V5.0) , SET 3(V7.5), SET 4(V10.0).

As shown in the Table 4.3, for each device the bandgap energy is different at each end. As it shown in fig.4.3, the FESEM image clearly presents that both end have different morphologies which was predicted as different concentration of Zn2+ ions at different region, that also may cause this effect.

This difference in bandgap also can be explained by defect formed in ZnO nanowires during the synthesis process. The applied voltage during the CBD effected the Zn2+ ions concentration having higher concentration at negative terminal region. ZnO nanowire is in general n type due to naturally occurring oxygen vacancies. There is another type of n type defect, which is zinc intrinsic. It may occur during the synthesis process in presence of excess Zn2+ because the zinc intrinsic defect formation energy is relatively low, thus there is a high possibility of this kind of defects.

4.3. Electrical Properties

The main target of this work is to fabricate a Chemiresistive sensing device based on ZnO nanowire grown on Silicon substrate, thus the electrical properties of the whole system was analyse from data collected about the Voltage – Current Characteristics of each device separately.

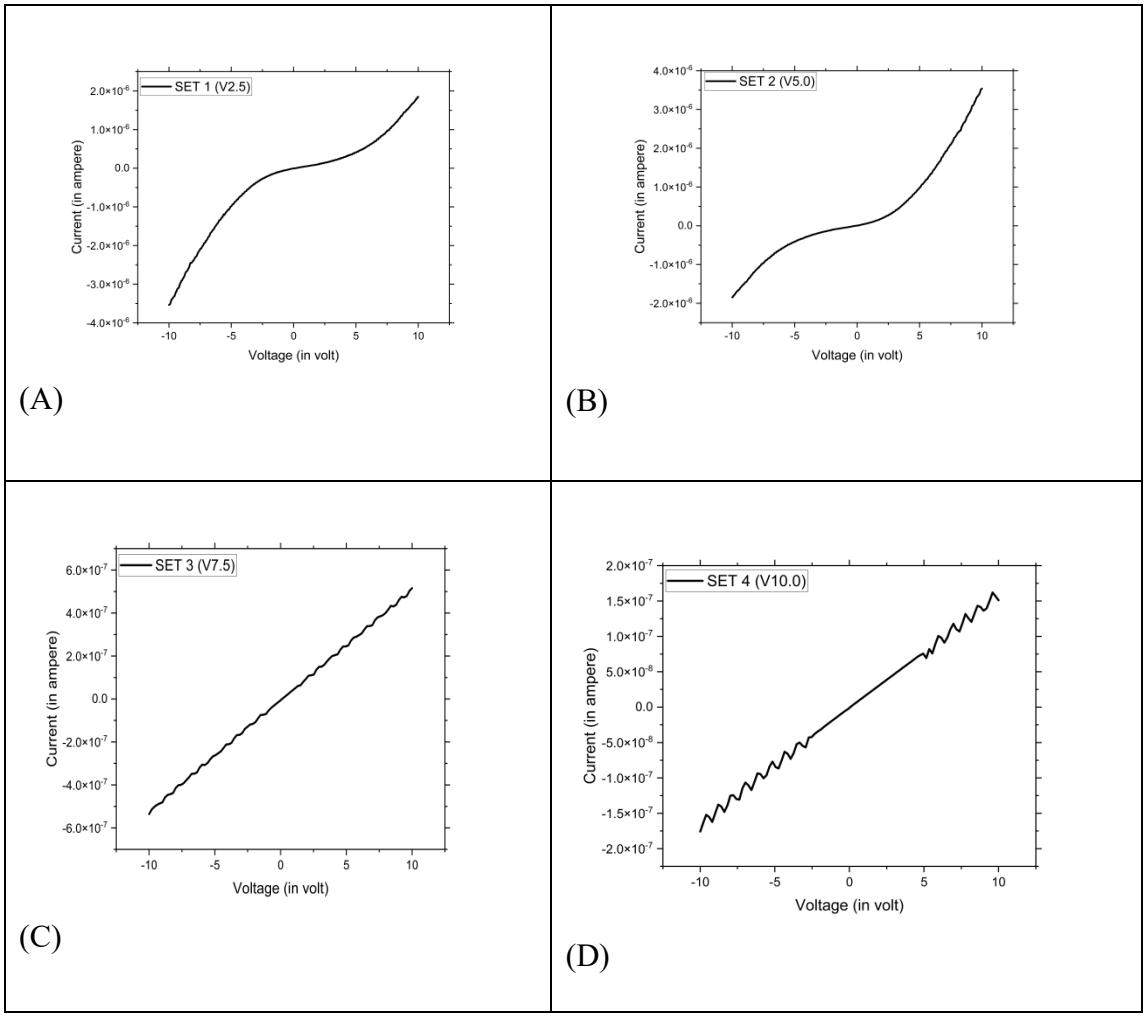


Fig 4.6 Voltage-current (I-V) characteristics of four devices

(A) SET 1(V2.5); (B) SET 2(V5.0); (C) SET 3(V7.5); (D) SET 4(V10.0)

The Fig 4.6 shows the voltage-current characteristics of those four devices within the range of +10V to -10V. From the plot it is clear that the device fabricated under applied voltage 2.5V show most nonlinearity. Even the device fabricated under 5.0V also showed nonlinearity but other 2 devices which are fabricated under 7.5V and 10.0V show no distinct nonlinearity.

To get a better understanding of the devices electrical nature a circuit was designed equivalent to the devices using Pspice software.

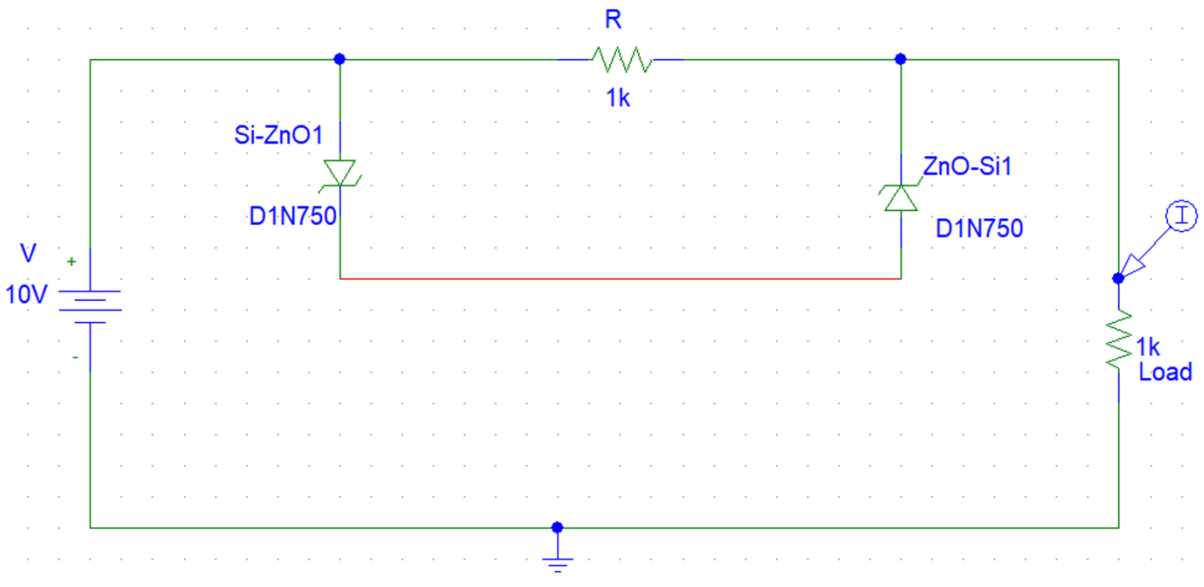


Fig 4.7 The drawing of the equivalent circuit of the device designed in Pspice software

A DC swipe in the range of +10V to -10V was taken of this design. The I-V characteristics plot was quite similar that of real device.

As shown in the Fig 4.7 the ZnO-Si interface at both ends was treated as Zener diode. To justify this assumption, another equivalent circuit was drawn and compared it with I-V characteristics data collected from 2 pieces of devises split at the middle, one of the probe was connected to ZnO surface and other Probe was connected to Silicon substrate.

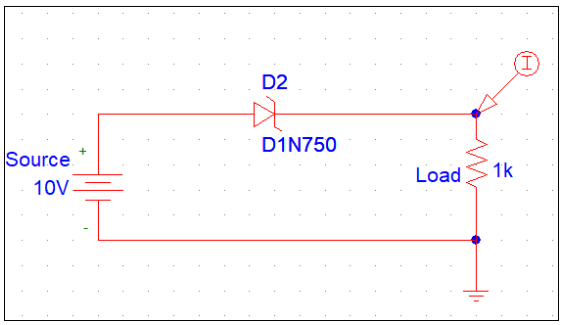


Fig 4.8 circuit design for I-V characteristics of a diode

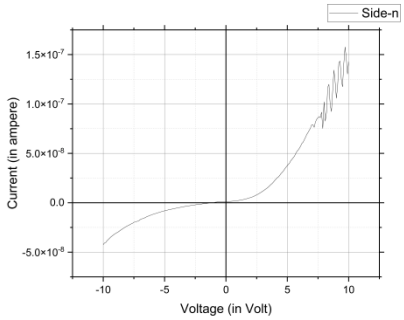
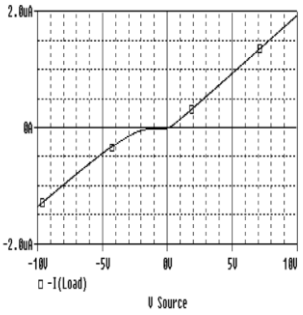
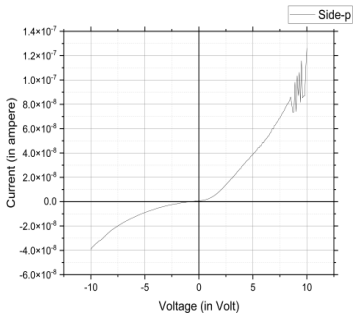
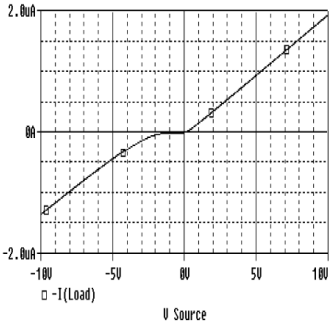
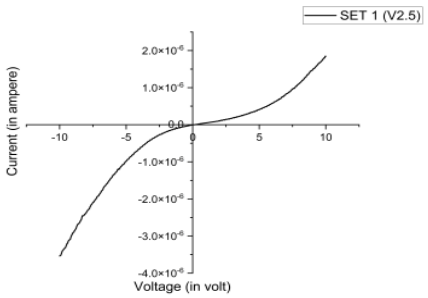
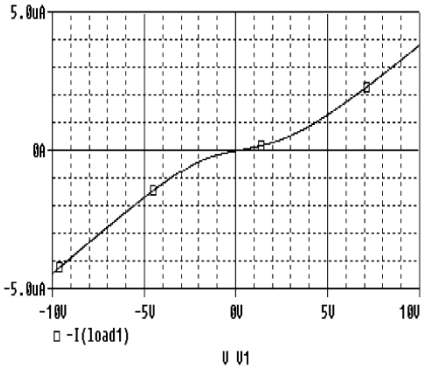
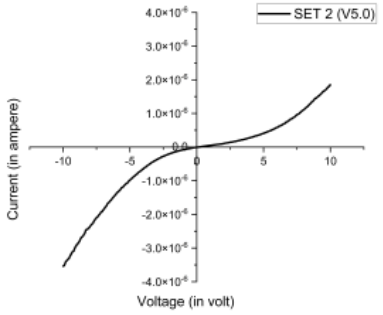
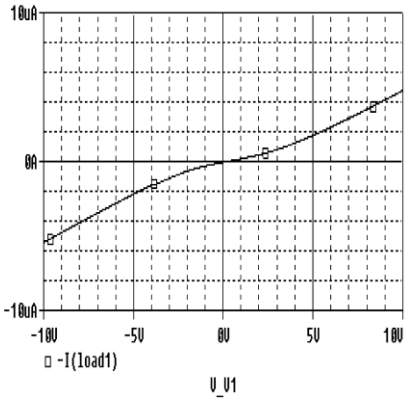
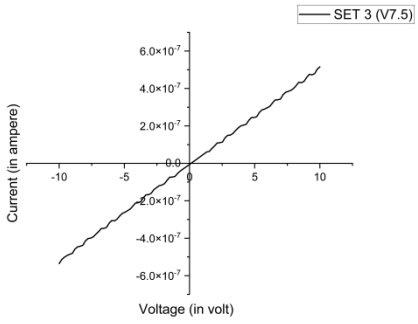
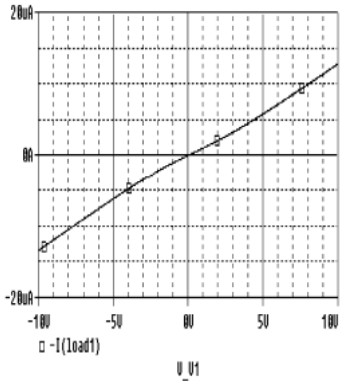
	I-V Characteristics	
	Data from real device	Data from equivalent circuit
End connected to negative terminal during fabrication		
End connected to positive terminal during fabrication		

Fig 4.9 comparative I-V characteristics equivalent circuit and the real device

From the Fig 4.9, it can be deducted that both end of the device may act like Zener diode.

Name	Voltage-Current Characteristics(IV plot)	
	Device Data(Measured at SMU)	Equivalent Circuit Data(pspice software)
SET 1(V2.5)		
SET 2(V5.0)		
SET 3(V7.5)		

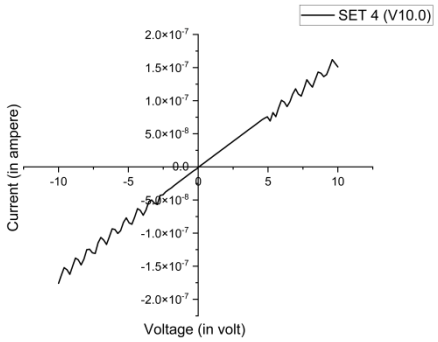
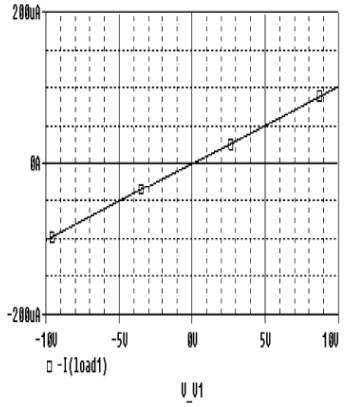
SET 4(V10.0)		

Table 4.4 comparison between IV characteristics of the devices and their equivalent circuit

In the pspice software, the data was collected for different Resistance such as 10^5, 10^6, 5*10^6, and 10^7 ohm. The plot drawn from the software data almost matches with the practical data collected from the devices.

From this comparison it can be concluded that when the voltage were differ to get the different devices, the resistance of the surface materials also increased.

4.4. Heavy Metal Detection

Here, the electrical performances of devices in the presence of few selective Heavy metal ions are investigated and analysed.

4.4.1. Chemiresistive sensing Analysis

As discussed in previous section, each of the devices (SET 1(V2.5); SET 2(V5.0); SET 3(V7.5); SET 4(V10.0)) were investigated separately in probe station in presence of 100ppm stock solution of Cu(II), Cr(III), Fe(III) and Ni(II) simultaneously.

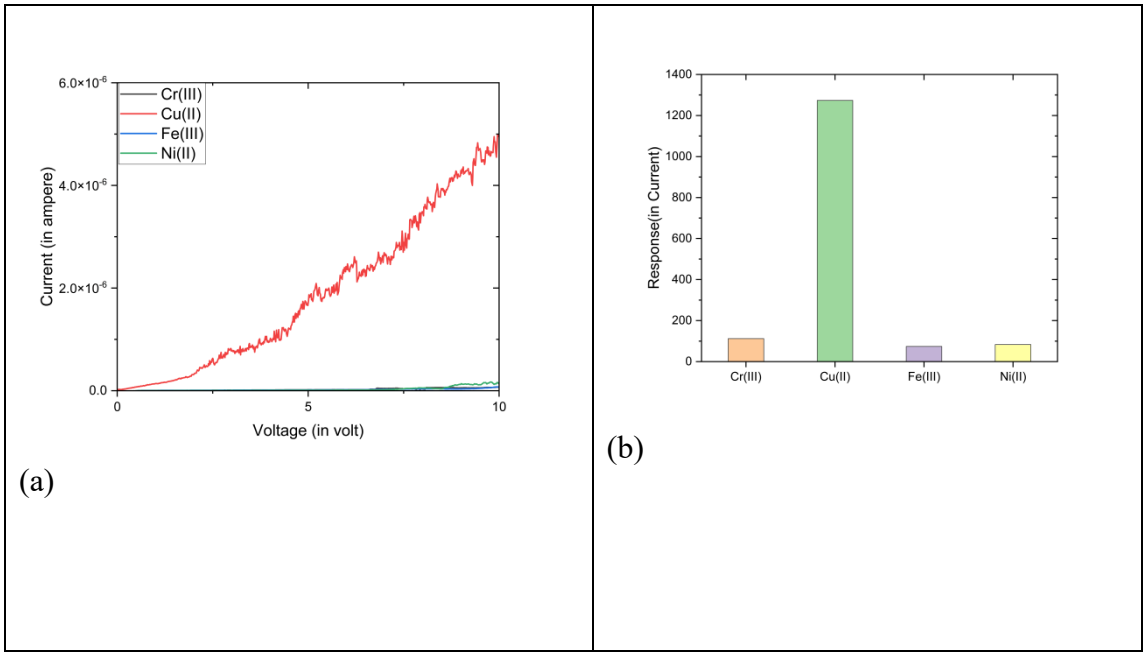


Fig 4.10 Cu(II), Cr(III), Fe(III) and Ni(II) sensing using SET 1(V2.5)

(a) Response, (b) Selectively

First of all, the device SET 1(V2.5) was tested. It showed quite high response in presence of Cu (II). As shown in the Fig4.8 the device has high selectivity towards the Cu (II) ion.

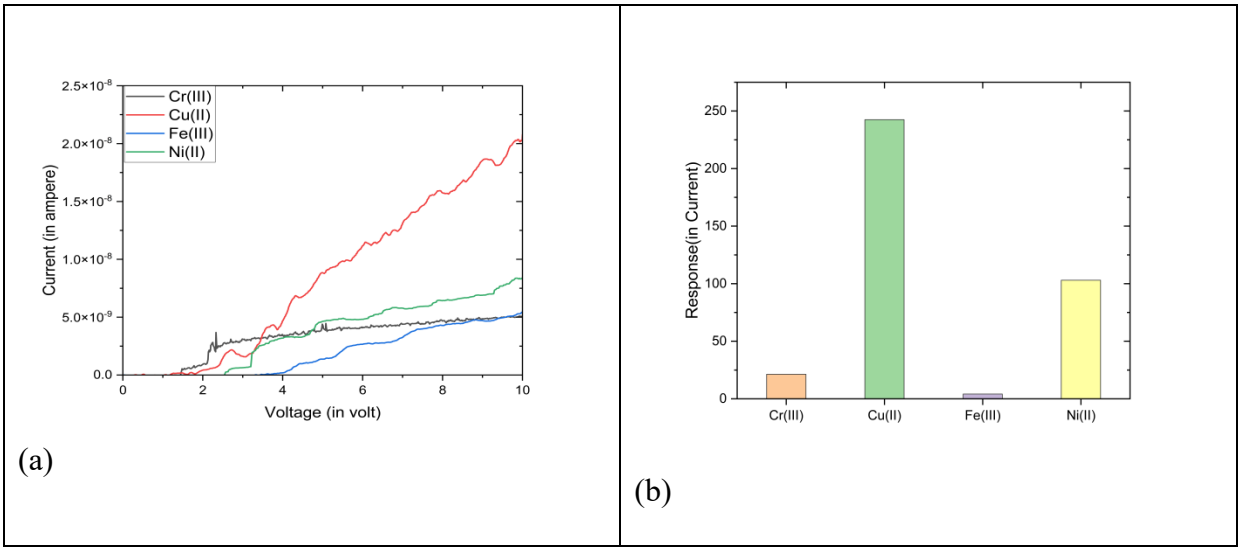


Fig 4.11 Cu(II), Cr(III), Fe(III) and Ni(II) sensing using SET 2(V5.0)

(b) Response, (b) Selectively

The Fig 4.11 shows the current response of the device SET 2 (V5.0) , it also shows relatively higher response toward Cu (II) in comparison with Cr(III), Fe(III) and Ni(II).

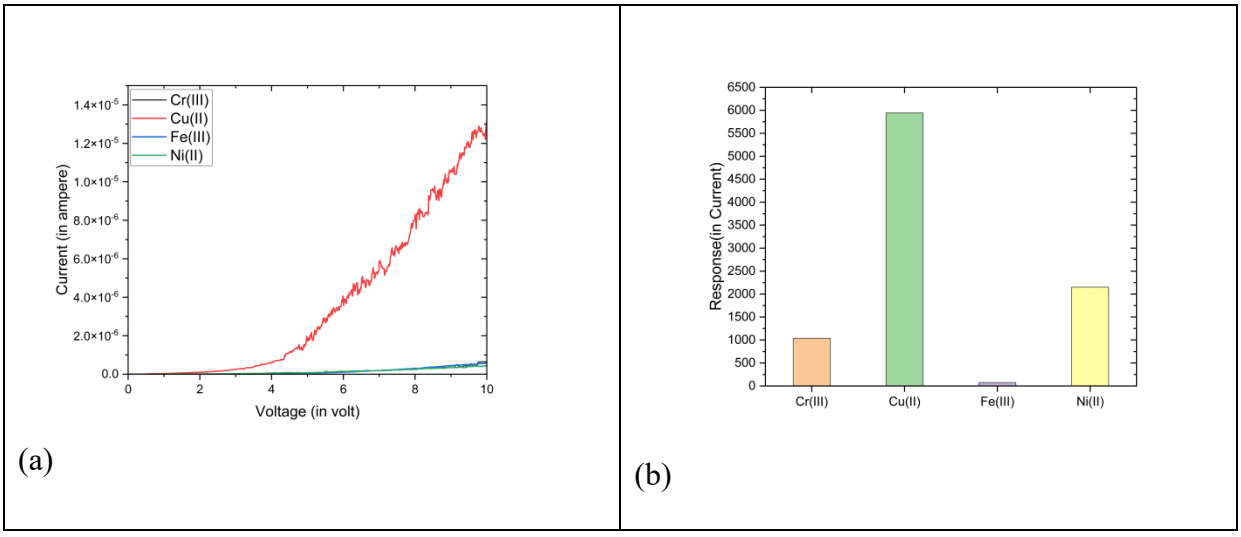


Fig 4.12 Cu(II), Cr(III), Fe(III) and Ni(II) sensing using SET 3(V7.5)

(c) Response, (b) Selectively

In case of SET 3(V7.5) the current response of the device in presence of Cu(II) is higher than the other devices. Also showed relative higher sensitivity towards Cu(II).

As shown in the fig 4.11 the device SET4(V10.0) has current response little lesser that that of previous device. Also shows relative high selectivity towards Cu(II).

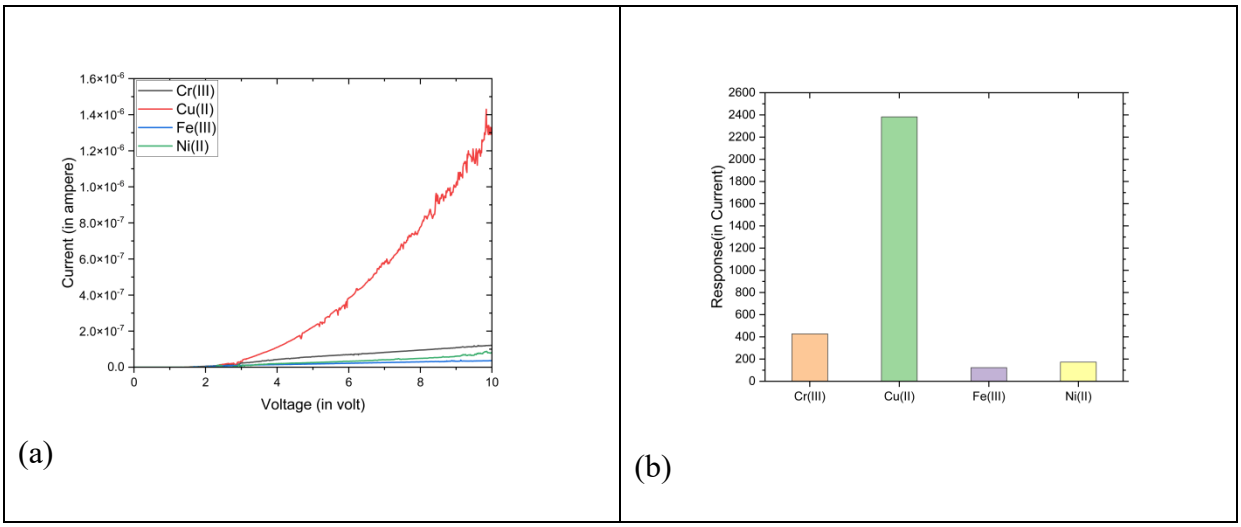


Fig 4.13 Cu(II), Cr(III), Fe(III) and Ni(II) sensing using SET 4(V10.0)

(a) Response, (b) Selectively

Analysing these data, it can be clearly concluded that the device fabricated by Voltage-assisted CBD using ZnO nanowire as a sensing material has a high selectivity towards Cu(II) during Chemiresistive sensing process.

The reason for this can be present as the interaction between ZnO and Cu(II). As the process was perform using aqueous solution, Liao et al.(112) showed in their work that ZnO nanoparticles can be hydroxylated in aqueous solution and creates a ZnOH2+ complex by coupling with H+. The H+ end is usually exposed at the interface end which further binds to water molecules, thus forming a positive interface. Wang et al. (113) also showed in their

work that the Cu(II) present in aq. Medium can form a weak bond with the oxygen present at the interface. Rajabi et al. (114) in their work explained how the aq. Cu(II) can further hydrolysed to have better adsorption at the interface.

Brad et al. (115) provided a list of standard potential of materials in aqueous medium. From that list the standard potential of the targeted heavy metals were collected

Heavy metal Ions	Standard reduction potential (v)
Cu(II)	0.159
Cr(III)	-0.424
Fe(II)	-0.44
Ni(II)	-0.257

Table 4.5 List of standard reduction potential of Cu(II), Cr(III), Fe(III) and Ni(II)

The list provided in the Table 4.5 clearly showed that Cu(II) as positive standard reduction potential, thus it is favourable for Cu2+ reduced into Cu.

As describe in section 4.3, the electrical properties of the device is related to the resistance of the surface. Now the adsorbed Cu(II) get reduced into Cu which is conductive thus decreases the resistance of the surface. This can justify the IV characteristics of the devices.

Also in air the device performance showed that device fabricated under 2.5 v , 5.0v, 7.5v and 10.0v have gradually increasing surface resistance. The relatively higher current response in the device fabricated under 7.5 v may be explained as it has higher relative adsorption of Cu(II) than other devices with respect to its surface resistance in air.

Chapter-:

CONCLUSION AND FUTURE WORK

7. CONCLUSION AND FUTURE WORK

In conclusion, this work presents a unique device fabrication method Voltage-assisted Chemical Bath Deposition (CBD) to synthesise ZnO Nanowire on Silicon substrate. The applied voltage was one of the growth parameters thus, by changing them while keeping other parameters same four devices were fabricated to study the effect of the applied voltage on the growth of ZnO nanowires.

In this work, a double CBD method was used to grow the ZnO nanowires. The target of first CBD was to grow a seed layer of ZnO upon which the ZnO nanowire can be grown following the seed layers' orientation. The second CBD was to grow the ZnO nanowires on the previously deposited growth layer.

XRD and FESEM imaging were performed on the devices to get morphological data on those devices. The XRD pattern shows 4 distinct planes of ZnO formed on the substrate, and the FESEM image showed different morphologies at different ends of the substrate.

DRS spectroscopy was also provided for optical property analysis. that data used to explain the effect of different applied voltage on ZnO nanowire grown caused a difference in energy bandgap at the opposite end of the devices

The I-V characteristics show the four different voltage-current relations between the four devices. The four devices showed different levels of nonlinear I-V characteristics as the applied voltage changed during the fabrication processes, which were explained using an equivalent circuit model.

The main target of this work was to use the fabricated device as a Chemiresistive sensor. To analyse the devices Chemiresistive performance, a few heavy metal ions i.e. Cu (II), Cr(III),Fe(II) and Ni(II) with 100 ppm concentration was used as control target. All of the devices showed high level of selectivity towards Cu (II). The four devices showed different levels of current response in the presence of those control targets. In this work, the possible reasons for those differences are also explained.

Future Works:

- There are many possibilities of the variation in energy bandgap within the devise, defect formation is one of them. To get a better understanding on the defect within the nanowires TEM data of those devices may help tremendously.
- To better explain the electrical nonlinearity of those devices the charge type and concentration data can be collected using Hall Probe method.
- ZnO nanowire has a wide range of effect due to presence of different dopant. So in future the fabrication process can be implemented using different dopant during growth process.
- The device can be also used as biosensor. Current study shows that different morphology of ZnO have different level of adsorption capability to different volatile organic compounds(VOCs) . This work showed that the devise has 2 distinct morphology in it and showed different level of adsorption at different growth condition thus it has positive possibility of performing as an excellent Chemiresistive VOC sensor.

Chapter-5:

REFERENCES

6. REFERENCES

1. Meng, Fanli, et al. "Detection of four alcohol homologue gases by ZnO gas sensor in dynamic interval temperature modulation mode." Sensors and Actuators B: Chemical 350 (2022): 130867.
2. Serhane, Rafik, et al. "Pulsed laser deposition of piezoelectric ZnO thin films for bulk acoustic wave devices." Applied Surface Science 288 (2014): 572-578.
3. Tang, Jian-Fu, et al. "Growth of dual-layer nanorods and nanowalls using Al reaction layer for cholesterol biosensor." IEEE Sensors Journal 17.6 (2017): 1584-1589.
4. Tang, Jian-Fu, et al. "ZnO nanowalls grown at low-temperature for electron collection in high-efficiency perovskite solar cells." Solar Energy Materials and Solar Cells 154 (2016): 18-22.
5. Tchounwou, P. B.; Yedjou, C. G.; Patlolla, A. K.; Sutton, D. J. Heavy Metals Toxicity and the Environment. In Molecular, Clinical and Environmental Toxicology; Luch, A., Ed.; Experientia Supplementum, Vol. 101; Springer: Berlin, Germany, 2012; pp 133–164. doi:10.1007/978-3-7643-8340-4_6
6. Singh, S.; Barick, K. C.; Bahadur, D. Nanomater. Nanotechnol. 2013, 3, 20. doi:10.5772/57237
7. Anjum, M.; Miandad, R.; Waqas, M.; Gehany, F.; Barakat, M. A. Arabian J. Chem., in press. doi:10.1016/j.arabjc.2016.10.004
8. C. Jagadish and S. J. Pearton, Zinc Oxide Bulk, Thin Films and Nanostructures, Elseviser Ltd., (2006).
9. B. Meyer, and D. Marx, Phys. Rev. B 2003, 67, 035403.
10. C. H. Bates, W. B. White, R. Roy, Science 1962, 137, 993.
11. C. Jagadish, and S. J. Pearton (eds.), Zinc Oxide Bulk, Thin Films, and Nanostructures (Elsevier, Amsterdam, 2006), p. 1.
12. Ü. Özgür, Ya. L. Alivov, C. Liu, A. Teke, M. Reshchikov, S. Dogan, V. Avrutin, S.J. Cho, and H. Morkoc, J. Appl. Phys. 2005, 98, 041301.
13. D. C. Look, Mater. Sci. Eng. 2001, 80, 383.
14. T. Olorunyolemi, A. Birnoim, Y. Carmel, O. Wilson, I. Lioyd, S. Smith, and R. Campbell, J. Am. Cera. Socie. 2002, 85, 1249.

15. D. I. Florescu, L. G. Mourokh, F. H. Pollak, D. C. Look, G. Cantwell, and X.Li, J. Appl. Phys. 2002, 91, 890.
16. N. H. Alvi, S. M. Usman Ali, S. Hussain, O. Nur, and M. Willander, Scripta Materialia 2011, 64, 697.
17. Ü. Özgür, Ya. L. Alivov, C. Liu, A. Teke, M. Reshchikov, S. Dogan, V. Avrutin, S.J. Cho, and H. Morkoc, J. Appl. Phys. 2005, 98, 041301.
18. A. B. Djurisic and Y. H. Leung, Small 2006, 2, 944.
19. X. Q. Meng, D. Z. Shen, J. Y. Zhang, D. X. Zhao, Y. M. Lu, L. Dong, Z. Z. Zhang, Y.C. Liu, X.W. Fan, Solid State Commun. 2005, 135, 179.
20. D. C. Look, Mater. Sci. Eng. 2001, 80, 383.
21. Y. Q. Chen, J. Jiang, Z. Y. He, Y. Su, D. Cai, L. Chen, Mater. Lett. 2005, 59, 3280. [26] P. H. Kasai, Phys. Rev. 1963, 130, 989.
22. K. Vanheusden, W. L. Warren, C. H. Seager, D. R. Tallant, J. A. Voigt, and B. E. Gnade, J. Appl. Phys. 1996, 79, 7983.
23. S. Yamauchi, Y. Goto, and T. Hariu, J. Cryst, Growth 2004, 260, 1.
24. X. Liu, X. Wu, H. Cao, and R. P. H. Chang, J. Appl. Phys. 2004, 95, 3141.
25. J. Zhong, A. H. Kitati, P. Mascher, and W. Puff, J. Electro. Chem. Soc. 1993, 140, 3644.
26. D. Li, Y. H. Leung, A. B. Djurisic, Z. T. Liu, M. H. Xie, S. L. Shi, S. J. Xu, and W. K. Chan, Appl. Phys. Lett. 2004, 85, 1601.
27. L. E. Greene, M. Law, J. Goldberger, F. Kim, J. C. Johnson, Y. Zhang, R. J. Saykally and P. Yang, Angew. Chem. Int. Edn. 2003, 42, 3031.
28. F. Tuomisto, K. Saarinen, D.C. Look, and G.C. Farlow, Phys. Rev. B 2005, 72, 085206
29. X. Yang, G. Du, X. Wang, J. Wang, B. Liu, Y. Zhang, D. Liu, D. Liu, H. C. Ong, and S.Yang, J. Cryst. Growth 2003, 252, 275.
30. M. Liu, A. H. Kitai, and P. Mascher, J. Lumin.1992, 54, 35.
31. E. G.Bylander, J. Appl. Phys.1978, 49, 188.
32. M. Gomi, N. Oohira, K.Ozaki, and M. Koyano, Japan. J. Appl. Phys. 2003, 42, 481.
33. K. Johnston, M. O. Henry, D. M. Cabe, T. Agne, and T. Wichert, Second Workshop on“SOXESS European Network on ZnO, 27-30 October 2004, Caernarfon, Wales, UK
34. A. Janotti, and C. G. Van de Walle, Phys. Rew. B 2007, 76, 165202.

35. T. Kogure, and Y. Bando, J. Electron Microsc. 1993, 47, 7903.
36. A. B. M. A. Ashrafi, A. Ueta, A. Avramescu, H. Kumano, I. Suemune, Y. W. Ok, and T.
37. Y. Seong, Appl. Phys. Lett. 2000, 76, 550.
38. Z. Fan, P. Chang, E. C. Walter, C. Lin, H. P. Lee, R. M. Penner, and J. G. Lu, Appl. Phys. Lett. 2004, 85, 6128
39. P. Klason, T. M. Borseth, Q. X. Zhao, B. G. Svensson, A. Y. Kuznetsov, and M. Willander, Sol. Stat. Commun. 2008, 145, 321. S. M. Usman Ali, N.H. Alvi, Z. Ibupoto, O. Nur, M. Willander, B. Danielsson, Sens. & Actuators :B 2011, 2, 241.
40. Z. Li, R. S. Yang, M. Yu, F. Bai, C. Li, and Z. L. Wang, J. Phys. Chem. C 2008, 112, 20114.
41. J. Zhou, N. S. Xu, and Z. L. Wang, Adv. Mater 2006, 18, 2432.
42. M. H. Asif, S.M. Usman Ali, O. Nur, M. Willander, C. Brännmark, P. Strålfors , U. Englund, F. Elinder and B. Danielsson, Biosens. Bioelectron.2010, 25, 2205.
43. S. A. Studenikin, N. Golego, and M. Cocivera, J. Appl. Phys. 1998, 84, 2287.
44. M. Razeghi, and A. Rogalski, J. Appl. Phys. 1996, 79, 7433
45. D. C. Look, B. Claflin, Y. I. Alivov, and S. J. Park, Phys. Stat. Sol. A2004, 201, 2203
46. *Look, D. C., Reynolds, D. C., et al.* (1999). "Characterization of ZnO films by Hall-effect measurements." *Applied Physics Letters*, 75(6), 811. DOI: 10.1063/1.124482.
47. *Janotti, A., & Van de Walle, C. G.* (2007). "Native point defects in ZnO." *Physical Review B*, 76(16), 165202. DOI: 10.1103/PhysRevB.76.165202.
48. *Lavrov, E. V., Herklotz, F., et al.* (2002). "Hydrogen-related defects in ZnO studied by infrared absorption spectroscopy." *Physical Review B*, 66(16), 165205. DOI: 10.1103/PhysRevB.66.165205.
49. *Vlasenko, L. S., & Watkins, G. D.* (2005). "Optical detection of electron paramagnetic resonance of hydrogen in ZnO." *Physical Review B*, 71(12), 125210. DOI: 10.1103/PhysRevB.71.125210.
50. *Wagner, A. J., & Pearton, S. J.* (2010). "Defects and p-type doping in ZnO." *Applied Physics Reviews*, 4(4), 041101. DOI: 10.1063/1.3530746.
51. *Tsukazaki, A., Ohtomo, A., et al.* (2005). "Repeated temperature modulation epitaxy for p-type doping and light-emitting diode based on ZnO." *Nature Materials*, 4(1), 42-46. DOI: 10.1038/nmat1276.

52. Kaur, G.; Mitra, A.; Yadav, K. L., Pulsed laser deposited Al-doped ZnO thin films for optical applications. *Prog. Nat. Sci.* **2015,** *25*, 12-21.
53. Solanki, R.; Collins, G. J., Laser induced deposition of zinc oxide. *Appl. Phys. Lett.* **1983,** *42*, 662-663.
54. Ellmer, K., Magnetron sputtering of transparent conductive zinc oxide. Relation between the sputtering parameters and the electronic properties. *J. Phys. D: Appl. Phys* **2000,** *33*, 17-32
55. Konstantinidis, S.; Hemberg, A.; Dauchot, J. P.; Hecq, M., Deposition of zinc oxide layers by high-power impulse magnetron sputtering. *J. Vac. Sci. Technol. B* **2007,** *25*.
56. Bagnall, D. M.; Chen, Y. F.; Shen, M. Y.; Zhu, Z.; Goto, T.; Yao, T., Room temperature excitonic stimulated emission from zinc oxide epilayers grown by plasma-assisted MBE. *J. Cryst. Growth* **1998,** *184/185*, 605-609
57. Suja, M.; Bashar, S. B.; Morshed, M. M.; Liu, J., Realization of Cu-Doped p-Type ZnO Thin Films by Molecular Beam Epitaxy. *ACS Appl Mater Interfaces* **2015,** *7*, 8894-9.
58. Zhao, C.; Chen, A.; Ji, X.; Zhu, Y.; Gui, X.; Huang, F.; Tang, Z., Growth of vertically aligned ZnO nanowire arrays on ZnO single crystals. *Mater. Lett.* **2015,** *154*, 40-43.
59. Tynell, T.; Karppinen, M., Atomic layer deposition of ZnO: a review. *Semicond. Sci. Technol.* **2014,** *29*.
60. Byrappa, K.; Yoshimura, M., *Handbook of Hydrothermal Technology*. William Andrew LLC: 2001; p 893.
61. Liu, B.; Zeng, H. C., Hydrothermal Synthesis of ZnO Nanorods in the Diameter Regime of 50 nm. *J. Am. Chem. Soc.* **2003,** *125*, 4430-4431.
62. Yu, J.; Yu, X., Hydrothermal Synthesis and Photocatalytic Activity of Zinc Oxide Hollow Spheres. *Environ. Sci. Technol.* **2008,** *42*, 4902-4907.
63. Byrappa, K.; Subramani, A. K.; Ananda, S.; Rai, K. M. L.; Dinesh, R.; Yoshimura, M., Photocatalytic degradation of rhodamine B dye using hydrothermally synthesized ZnO. *Bull. Mater. Sci.* **2006,** *29*, 433-438.
64. Hodes, G., Semiconductor and ceramic nanoparticle films deposited by chemical bath deposition. *Phys Chem Chem Phys* **2007,** *9*, 2181-96.

65. Greene, L. E.; Law, M.; Tan, D. H.; Montano, M.; Goldberger, J.; Somorjai, G.; Yang, P., General Route to Vertical ZnO Nanowire Arrays Using Textured ZnO Seeds. *Nano Letters* **2005,** *5*, 1231-1236.
66. Pradhan, B.; Batabyal, S. K.; Pal, A. J., Vertically aligned ZnO nanowire arrays in Rose Bengal-based dye-sensitized solar cells. *Sol. Energy Mater. Sol. Cells* **2007,** *91*, 769-773.
67. Lin, Y.; Jiang, Q., Effect of substrates and anions of zinc salts on the morphology of ZnO nanostructures. *Appl. Surf. Sci.* **2011,** *257*, 8728-8731.
68. Akgun, M. C.; Afal, A.; Unalan, H. E., Hydrothermal zinc oxide nanowire growth with different zinc salts. *J. Mater. Res.* **2012,** *27*, 2401-2407.
69. Jung, J.; Myoung, J.; Lim, S., Effects of ZnO nanowire synthesis parameters on the photovoltaic performance of dye-sensitized solar cells. *Thin Solid Films* **2012,** *520*, 5779-5789.
70. Strano, V.; Urso, R. G.; Scuderi, M.; Iwu, K. O.; Simone, F.; Ciliberto, E.; Spinella, C.; Mirabella, S., Double Role of HMTA in ZnO Nanorods Grown by Chemical Bath Deposition. *J. Phys. Chem. C* **2014,** *118*, 28189-28195.
71. Solís-Pomar, F.; Martínez, E.; Meléndrez, M. F.; Pérez-Tijerina, E., Growth of vertically aligned ZnO nanorods using textured ZnO films. *Nanoscale Res. Lett.* **2011,** *6*, 1-11.
72. Parize, R.; Garnier, J.; Chaix-Pluchery, O.; Verrier, C.; Appert, E.; Consonni, V., Effects of Hexamethylenetetramine on the Nucleation and Radial Growth of ZnO Nanowires by Chemical Bath Deposition. *J. Phys. Chem. C* **2016,** *120*, 5242-5250.
73. Baruah, S.; Dutta, J., pH-dependent growth of zinc oxide nanorods. *J. Cryst. Growth* **2009,** *311*, 2549-2554.
74. Verrier, C.; Appert, E.; Chaix-Pluchery, O.; Rapenne, L.; Rafhay, Q.; Kaminski-Cachopo, A.; Consonni, V., Effects of the pH on the Formation and Doping Mechanisms of ZnO Nanowires Using Aluminum Nitrate and Ammonia. *Inorg Chem* **2017,** *56*, 13111-13122.
75. Q. Zhang, C. S. Dandeneau, X. Zhou, and C. Cao, "ZnO nanostructures for dye-sensitized solar cells," Advanced Materials, vol. 21, no. 41, pp. 4087–4108, 2009.
76. H. M. Cheng, W. H. Chiu, C. H. Lee, S. Y. Tsai, and W.F. Hsieh, "Formation of branched ZnO nanowires from solvothermal method and dye-sensitized solar cells

applications," Journal of Physical Chemistry C, vol. 112, no. 42, pp. 16359–16364, 2008.

77. S. H. Ko, D. Lee, H. W. Kang et al., "Nanoforest of hydrothermally grown hierarchical ZnO nanowires for a high efficiency dye-sensitized solar cell," Nano Letters, vol. 11, no. 2, pp. 666–671, 2011.
78. J. Zhong, H. Chen, G. Saraf et al., "Integrated ZnO nanotips on GaN light emitting diodes for enhanced emission efficiency," Applied Physics Letters, vol. 90, no. 20, Article ID 203515, 2007.
79. C. H. Chen, S. J. Chang, S. P. Chang et al., "Electroluminescence from n-ZnO nanowires/p-GaN heterostructure lightemitting diodes," Applied Physics Letters, vol. 95, no. 22, Article ID 223101, 2009.
80. X. M. Zhang, M. Y. Lu, Y. Zhang, L. J. Chen, and Z. L.Wang, "Fabrication of a high-brightness blue-light-emitting diode using a ZnO-Nanowire array grown on p-GaN thin film," Advanced Materials, vol. 21, no. 27, pp. 2767–2770, 2009.
81. C. Y. Lu, S. P. Chang, S. J. Chang et al., "A lateral ZnO nanowire UV photodetector prepared on a ZnO:Ga/glasstemplate," Semiconductor Science and Technology, vol. 24, no. 7, Article ID 075005, 2009.
82. K. J. Chen, F. Y. Hung, S. J. Chang, and S. J. Young, "Optoelectronic characteristics of UV photodetector based on ZnO nanowire thin films," Journal of Alloys and Compounds, vol. 479, no. 1-2, pp. 674–677, 2009.
83. Y. Li, F. D. Valle, M. Simonnet, I. Yamada, and J. J. Delaunay, "High-performance UV detector made of ultra-long ZnO bridging nanowires," Nanotechnology, vol. 20, no. 4, Article ID 045501, 2009.
84. Z. L. Wang and J. Song, "Piezoelectric nanogenerators based on zinc oxide nanowire arrays," Science, vol. 312, no. 5771, pp. 242–246, 2006.
85. X. Wang, J. Song, J. Liu, and L. W. Zhong, "Direct-current nanogenerator driven by ultrasonic waves," Science, vol. 316, no. 5821, pp. 102–105, 2007.
86. G. Zhu, R. Yang, S. Wang, and Z. L. Wang, "Flexible highoutput nanogenerator based on lateral ZnO nanowire array," Nano Letters, vol. 10, no. 8, pp. 3151–3155, 2010.
87. Y. Hu, C. Xu, Y. Zhang, L. Lin, R. L. Snyder, and Z. L. Wang, "A Nanogenerator for energy harvesting from a rotating tire and its application as a self-powered pressure/speed sensor," Advanced Materials, vol. 23, pp. 4068–4071, 2011.

88. J. O. Hwang, D. H. Lee, J. Y. Kim et al., “Vertical ZnO nanowires/graphene hybrids for transparent and flexible field emission,” Journal of Materials Chemistry, vol. 21, no. 10, pp. 3432–3437, 2011.
89. C. H. Chen, S. J. Chang, S. P. Chang et al., “Enhanced field emission of well-aligned ZnO nanowire arrays illuminated by UV,” Chemical Physics Letters, vol. 490, no. 4–6, pp. 176–179, 2010.
90. A. Sugunan, V. K. Guduru, A. Uheida, M. S. Toprak, and M. Muhammed, “Radially oriented ZnO nanowires on flexible poly-L-lactide nanofibers for continuous-flow photocatalytic water purification,” Journal of the American Ceramic Society, vol. 93, no. 11, pp. 3740–3744, 2010.
91. T. J. Kuo, C. N. Lin, C. L. Kuo, and M. H. Huang, “Growth of ultralong ZnO nanowires on silicon substrates by vapor transport and their use as recyclable photocatalysts,” Chemistry of Materials, vol. 19, no. 21, pp. 5143–5147, 2007.
92. L. Li, H. Yang, H. Zhao et al., “Hydrothermal synthesis and gas sensing properties of single-crystalline ultralong ZnO nanowires,” Applied Physics A, vol. 98, no. 3, pp. 635–641, 2010
93. V. P. Verma, S. Das, S. Hwang, H. Choi, M. Jeon, and W. Choi, “Nitric oxide gas sensing at room temperature by functionalized single zinc oxide nanowire,” Materials Science and Engineering B, vol. 171, no. 1–3, pp. 45–49, 2010.
94. C. W. Na, H. S. Woo, I. D. Kim, and J. H. Lee, “Selective detection of NO2 and C2H5OH using a CO3O4-decorated ZnO nanowire network sensor,” Chemical Communications, vol. 47, no. 18, pp. 5148–5150, 2011.
95. J. Y. Park, Y. K. Park, and S. S. Kim, “Formation of networked ZnO nanowires by vapor phase growth and their sensing properties with respect to CO,” Materials Letters, vol. 65, no. 17-18, pp. 2755–2757, 2011.
96. I. C. Yao, P. Lin, and T. Y. Tseng, “Hydrogen gas sensors using ZnO-SNO2 core-shell nanostructure,” Advanced Science Let- ters, vol. 3, no. 4, pp. 548–553, 2010.
97. X. Zhou, J. Li, M. Ma, and Q. Xue, “Effect of ethanol gas on the electrical properties of ZnO nanorods,” Physica E, vol. 43, no. 5, pp. 1056–1060, 2011
98. A. Fulati, S. M. U. Ali, M. H. Asif et al., “An intracellular glucose biosensor based on nanoflake ZnO,” Sensors and Actuators, B, vol. 150, no. 2, pp. 673–680, 2010

99. X. Liu, Q. Hu, Q. Wu, W. Zhang, Z. Fang, and Q. Xie, “Aligned ZnO nanorods: a useful film to fabricate ampero- metric glucose biosensor,” Colloids and Surfaces B, vol. 74, no. 1, pp. 154–158, 2009.
100. A. Choi, K. Kim, H. I. Jung, and S. Y. Lee, “ZnO nanowire biosensors for detection of biomolecular interactions in enhancement mode,” Sensors and Actuators, B, vol. 148, no. 2, pp. 577–582, 2010.
101. Franco, Mariane A., et al. "A review on chemiresistive ZnO gas sensors." *Sensors and Actuators Reports* 4 (2022): 100100.
102. M. Li, H. Gou, I. Al-Ogaidi, and N. Wu, "Nanostructured sensors for detection of heavy metals: a review," ed: ACS Publications, 2013.
103. M. E. Mahmoud, I. Kenawy, M. A. Hafez, and R. Lashein, "Removal, preconcentration and determination of trace heavy metal ions in water samples by AAS via chemically modified silica gel N-(1-carboxy-6-hydroxy) benzylidenepropylamine ion exchanger," Desalination, vol. 250, no. 1, pp. 62-70, 2010.
104. A. Nigam, N. Sharma, S. Tripathy, and M. Kumar, "Development of semiconductor based heavy metal ion sensors for water analysis: A review," Sensors and Actuators A: Physical, vol. 330, p. 112879, 2021.
105. X. Xu, S. Yang, Y. Wang, and K. Qian, "Nanomaterial-based sensors and strategies for heavy metal ion detection," Green Analytical Chemistry, vol. 2, p. 100020, 2022.
106. A. G.-M. Ferrari, P. Carrington, S. J. Rowley-Neale, and C. E. Banks, "Recent advances in portable heavy metal electrochemical sensing platforms," Environmental Science: Water Research & Technology, vol. 6, no. 10, pp. 2676-2690, 2020.
107. U. O. Aigbe et al., "Electrochemical Detection of Heavy Metals," Modified Nanomaterials for Environmental Applications: Electrochemical Synthesis, Characterization, and Properties, pp. 25-63, 2022.
108. Holzwarth, Uwe, and Neil Gibson. "The Scherrer equation versus the'Debye-Scherrer equation'." Nature nanotechnology 6.9 (2011): 534-534.
109. Hassanzadeh-Tabrizi, S. A. "Precise calculation of crystallite size of nanomaterials: A review." Journal of Alloys and Compounds (2023): 171914.
110. Makuła, Patrycja, Michał Pacia, and Wojciech Macyk. "How to correctly determine the band gap energy of modified semiconductor photocatalysts based on UV–Vis spectra." The journal of physical chemistry letters 9.23 (2018): 6814-6817.

111. Krasovska, Marina, et al. "ZnO-nanostructure-based electrochemical sensor: Effect of nanostructure morphology on the sensing of heavy metal ions." Beilstein journal of nanotechnology 9.1 (2018): 2421-2431.
112. Liao, Min-Hung, Chih-Hsiung Hsu, and Dong-Hwang Chen. "Preparation and properties of amorphous titania-coated zinc oxide nanoparticles." Journal of Solid State Chemistry 179.7 (2006): 2020-2026.
113. Wang, Xianbiao, et al. "Mass production of micro/nanostructured porous ZnO plates and their strong structurally enhanced and selective adsorption performance for environmental remediation." Journal of Materials Chemistry 20.39 (2010): 8582-8590.
114. Rajabi, Hamid, et al. "Nano-ZnO embedded mixed matrix polyethersulfone (PES) membrane: Influence of nanofiller shape on characterization and fouling resistance." Applied Surface Science 349 (2015): 66-77.
115. Bard, AllenJ. Standard potentials in aqueous solution. Routledge, 2017.
116. Pankove, Jacques I. Optical processes in semiconductors. Courier Corporation, 1975.
117. Kubelka, Paul, and F. R. A. N. Z. Munk. "A contribution to the optics of pigments." Z. Tech. Phys 12.593 (1931): 193.